1N, 0P, 1P) on the central unit and its neighbors ($j = i - 1, i, i + 1$) for time $s \le t$. Using the data obtained from our MC simulations, it appears that the ratio of the combinatory probability to the central state probability can be accurately approximated as a function of ${}^t\langle[\mu][\beta][\nu]\rangle_i$ defined by the following equation with the parameter τ representing the memory time length.

$$ {}^t\langle[\mu][\beta][\nu]\rangle_i = \frac{1}{\tau}\int_{-\infty}^{t} \exp\left(-\frac{t-s}{\tau}\right) {}^s[\mu]_{i-1}\,{}^s[\beta]_i\,{}^s[\nu]_{i+1}\,ds, $$
$$ \beta, \mu, \nu = 0\text{N}, 1\text{N}, 1\text{P} \text{ or } 0\text{P} \qquad (20) $$

The memory time length τ has a significant influence on the accuracy of the model, thus an optimal value of $\tau = 66.7$ ms was used for the set of transition rate parameters given in Table 1.

In our ODE model, the function to approximate the combinatory probability is given by:

$$ \frac{{}^t[\xi,\alpha,\eta]_i}{{}^t[\alpha]_i} \approx \exp\left(\sum_{\mu,\beta,\nu=0\text{N},1\text{N},1\text{P},0\text{P}} C(i)^{\mu,\beta,\nu}_{\xi,\alpha,\eta}\,{}^t\langle[\mu][\beta][\nu]\rangle_i\right). \qquad (21) $$

$C(i)^{\mu,\beta,\nu}_{\xi,\alpha,\eta}$ are parameters determined from the MC simulation results to attain the best approximations (Eq. (21)). $C(i)^{\mu,\beta,\nu}_{\xi,\alpha,\eta}$ values were determined by the least square fitting that minimizes the following approximate error ${}^tR$ over the duration of the MC simulation $[T_0{:}T_1]$.

$$ {}^tR(\xi,\alpha,\eta,i) = \log\frac{{}^t[\xi,\alpha,\eta]_i}{{}^t[\alpha]_i} - \sum_{\mu,\beta,\nu=0\text{N},1\text{N},1\text{P},0\text{P}} C(i)^{\mu,\beta,\nu}_{\xi,\alpha,\eta}\,{}^t\langle[\mu][\beta][\nu]\rangle \qquad (22) $$

To evaluate the probabilities (the argument of the first term on the right hand side of Eq. (22)), the data obtained from the MC simulations for the duration $[T_0{:}T_1]$ was divided into bins of equal time intervals ($DT = 2.5$ ms) and, in each bin, the number of distinct combinatory states (ξ_{i-1}, α_i, η_{i+1}) was counted at each time step ($\Delta t = 2.5$ μs) for each individual MH_i.

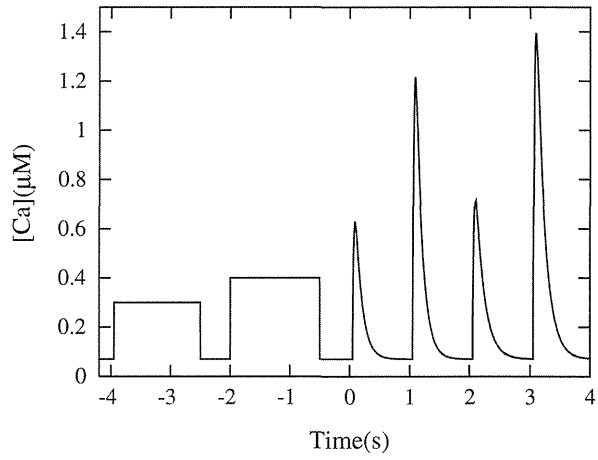

FIGURE 3. Ca-transients applied for the determination of ODE parameters. The last four were generated using the equation by Rice *et al.*[20] with the parameter set listed in Appendix.

The MC simulations were performed with various wave forms (Fig. 3) to cover the wide range of conditions.

Once the parameters $\left(C(i)^{\mu,\beta,\nu}_{\xi,\alpha,\eta}\right)$ are determined, ODE simulations can be performed by approximating the combinatory probabilities in Eq. (19) by

$$ {}^t\mathbf{p}_i^{\xi,\eta} \approx {}^t\mathbf{W}_i(\xi,\eta)\cdot{}^t\mathbf{p}_i \qquad (23) $$

with

$$ {}^t\mathbf{W}_i(\xi,\eta) = \begin{bmatrix} {}^tW(\xi,\,0\text{N},\,\eta,i) & 0 & 0 & 0 \\ 0 & {}^tW(\xi,\,1\text{N},\,\eta,i) & 0 & 0 \\ 0 & 0 & {}^tW(\xi,\,1\text{P},\,\eta,i) & 0 \\ 0 & 0 & 0 & {}^tW(\xi,\,0\text{P},\,\eta,i) \end{bmatrix}, \qquad (24) $$

where the diagonal entries are computed from

$$ {}^tW(\xi,\alpha,\eta,i) = \exp\left(\min\left(0, \sum_{\mu,\beta,\nu=0\text{N},1\text{N},1\text{P},0\text{P}} C(i)^{\mu,\beta,\nu}_{\xi,\alpha,\eta}\,{}^t\langle[\mu][\beta][\nu]\rangle_i\right)\right). \qquad (25) $$

Here, the minimum was applied so that ${}^t[\xi,\alpha,\eta]_i \le {}^t[\alpha]_i$ is fulfilled in any case. Finally, by substituting ${}^t\mathbf{p}_i^{\xi,\eta}$ in Eq. (19) with the approximations in Eq. (23), we obtain an ODE:

$$ \frac{d^t\mathbf{p}_i}{dt} = \sum_{\xi,\eta=\text{N},\text{P}} {}^t\mathbf{A}_i(\xi,\eta)\cdot{}^t\mathbf{W}_i(\xi,\eta)\cdot{}^t\mathbf{p}_i \equiv {}^t\mathbf{B}_i\cdot{}^t\mathbf{p}_i, \quad i = 1,\ldots,nu, \qquad (26) $$

where the 4 × 4 matrix ${}^{t}\mathbf{B}_i$ is given by

$$ {}^{t}\mathbf{B}_i = \sum_{\xi,\eta=\mathrm{N,P}} {}^{t}\mathbf{A}_i(\xi,\eta)\cdot {}^{t}\mathbf{W}_i(\xi,\eta). \qquad (27) $$

The validity of this conceptual framework was supported by the excellent predictive power of the ODE model. Although there is no theoretical reason for adopting the exponential function in Eq. (21), we empirically found this style of function enhanced the approximation of temporal rate changes, especially for values close to zero.

Details of the determination and estimation of the ODE parameters are shown in the Appendix.

Interpolation of the ODE Parameters for the Simulations of Shortening Contraction

As previously shown, the parameters $C(i)^{\mu,\beta,\nu}_{\xi,\alpha,\eta}$ can be estimated for individual MHs at a fixed *SL*. For the ODE simulation of shortening contraction where the *SL* is continuously changing, we adopted an interpolation method that uses the parameter values obtained at multiple *SL*'s $\{SL_0, SL_1,\ldots,SL_{NSL}\}$ with a constant interval $\Delta SL = SL_k - SL_{k-1}$. Namely, for any *SL* between SL_0 and SL_{NSL}:

$$ C(i)^{\mu,\beta,\nu}_{\xi,\alpha,\eta} = (1-\eta)C(SL_{k-1},i)^{\mu,\beta,\nu}_{\xi,\alpha,\eta} + \eta C(SL_k,i)^{\mu,\beta,\nu}_{\xi,\alpha,\eta} $$
$$ \text{for } SL_{k-1} \le SL \le SL_k,\ \ SL = (1-\eta)SL_{k-1} + \eta SL_k, \qquad (28) $$

In this study, $\Delta SL = 0.05$ μm was adopted.

Computation

To reduce computational costs, the transition matrices ${}^{t}\mathbf{A}_i(\xi, \eta)$ in Eq. (12) and ${}^{t}\mathbf{B}_i$ in Eq. (27) (only for ODE) are updated only at 0.25 ms intervals, whereas the MC states and ODE solutions are updated at 2.5 μs intervals. Such a treatment significantly reduces the computational time for MC and ODE simulations without introducing recognizable error.

The MC and ODE simulation codes were written and executed using Fortran90 on a single core of Intel Xeon X7560 (2.27 GHz). The total number of MHs was 36. Using this previously described protocol, the computation of one sample of the MC simulation took 0.82 s per one second time length. To obtain reasonable mean values, more than a thousand MC samples were required. In contrast, an ODE that used the approximation given in Eqs. (19), (23) and (24) took 0.64 s per one second time length. Thus, the ODE model allowed a great reduction in computational time.

RESULTS

Monte Carlo Simulation

In Fig. 4, the results from the MC simulations under steady-state condition are shown for force (in the following text, we use the fraction of bound cross-bridges [P](=[0P] + [1P]) as an index of developed force)–*SL* relations (Fig. 4a) and [P]–pCa relations (Fig. 4b). [P]–pCa relation clearly demonstrated a significant increase in the maximum Ca^{2+}-activated force and increased Ca^{2+}-sensitivity (a leftward shift of $[Ca_{50}]$) at longer *SL*s (see also Table 2), which is consistent with previous reports.[5,14] The Hill coefficient decreased a little at short *SL*s, but its *SL* dependence was much

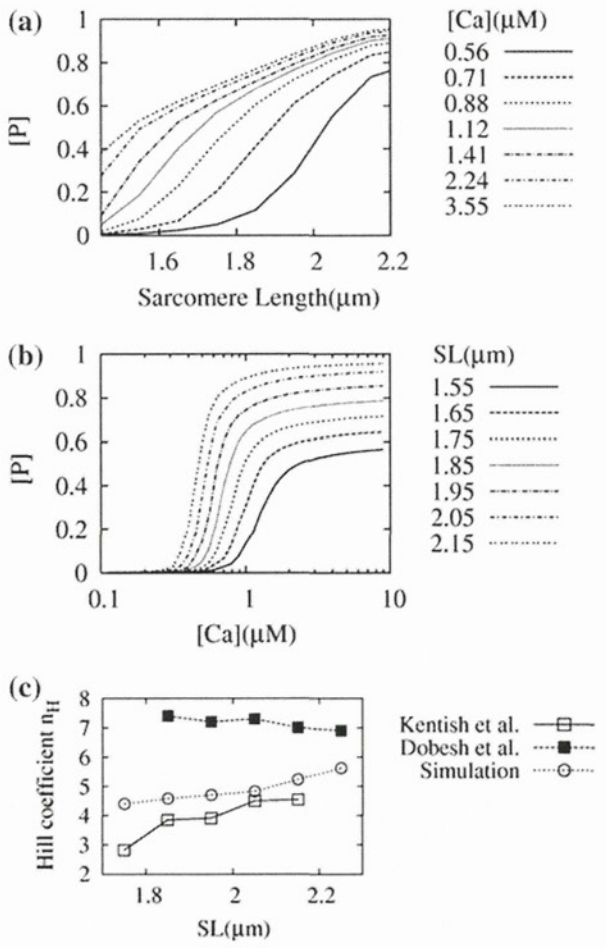

FIGURE 4. Results of MC simulation. Simulation was performed under constant Ca concentration and *SL* for 800 s (3.2×10^8 steps). Data from the equilibrium phase (400–800 s) were averaged. The number of the P-state (0P + 1P) was assumed as the index of force. (a) Force–length (*SL*) relations shown for different Ca concentrations ranging from 0.56 to 3.55 μM. (b) [P]–pCa relations obtained for different *SL*s ranging from 1.45 to 2.15 μm. (c) *SL* dependence of the Hill coefficient. Simulation results (closed circle) were compared with the experimental results by Kentish *et al.*[14] (open square) and Dobesh *et al.*[5] (closed square).

smaller than that reported by Kentish *et al.*[14] and closer to the recent results reported by Dobesh *et al.*[5] (Fig. 4c). Data were not available for the shorter range of *SL*s in either of these experimental studies.

Estimates of the ODE Parameters

The estimation of $\sum C(i)^{\mu,\beta,\nu}_{\xi,\alpha,\eta}\ {}^{t}\langle[\mu][\beta][\nu]\rangle_i$ in Eq. (22) was performed using the least square results of $nu = 36$ for each *SL*. MC simulation data were obtained from 10,000 samples for the Ca-transient that consists of the six peaks (Fig. 3). The results of this estimation analysis are shown for the units in the middle (MH_{18}) and near the filament edge (MH_5) at *SL* = 2.2 μm, in Fig. 5. Comparing the estimated values of $\left(\sum C(i)^{\mu,\beta,\nu}_{\xi,\alpha,\eta}\ {}^{t}\langle[\mu][\beta][\nu]\rangle_i\right)$ with the log $\left({}^{t}[\xi,\ \alpha,\ \eta]_i/{}^{t}[\alpha]_i\right)$ (Eq. (22)) obtained from the MC simulations, fairly good approximations are attained overall, for all combinations of the indices and the units. However, we found variations that were dependent on the location of the units. For example, observing the unit located in the middle of the filament (MF_{18}), the plots for ξ, η = P, N and ξ, η = N, P in each of its states (0N, 1N, 1P, and 0P) (middle two rows of Fig. 5a) show similar patterns because of the unit's symmetrical position along the filament, whereas the corresponding plots for the unit near the edge (MF_5) (middle two rows of Fig. 5b) show considerable differences. These findings indicate that the present estimation model is capable of capturing heterogeneous trends, which the models with the ring arrangement of the units[3,19] cannot reproduce.

Furthermore, wide variation is found in the values of $\log {}^{t}W(\xi, \alpha, \eta, i)$, supporting the use of a logarithmic scale when the close examination of ${}^{t}W(\xi, \alpha, \eta, i)$ is required.

TABLE 2. Fitted Hill equation parameters for the MC simulation data.

SL (μm)	$[P]_{max}$	$[Ca_{50}]$ (μM)	Hill coefficient n_H
1.55	0.567	1.40	3.96
1.65	0.645	1.12	4.29
1.75	0.716	0.94	4.40
1.85	0.787	0.81	4.58
1.95	0.856	0.70	4.70
2.05	0.920	0.61	4.82
2.15	0.957	0.53	5.23
2.25	0.967	0.50	5.62

Comparing the ODE Model and MC Simulation Results

The ODE (Eq. (19)) was simulated using the approximations in Eqs. (23) and (24) to obtain the temporal changes of the fraction of bound cross-bridges

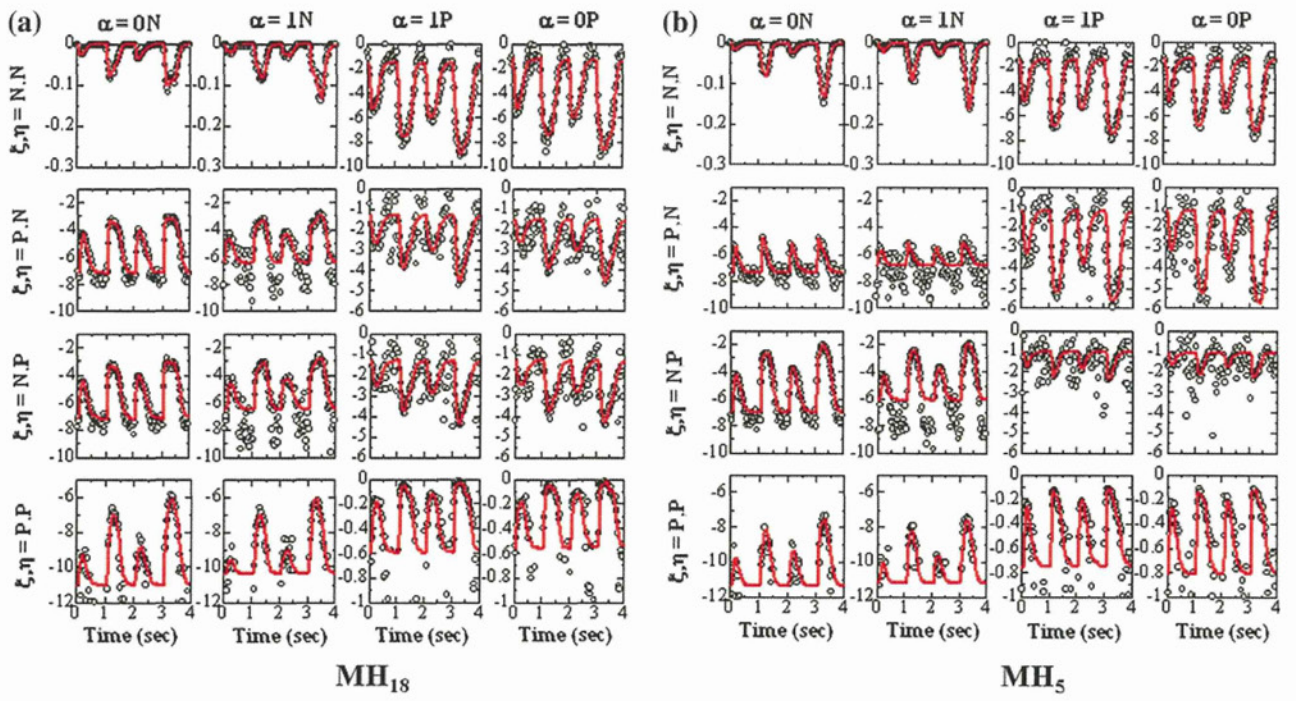

FIGURE 5. The least square fitting of the parameters. The values of $\sum C(i)^{\mu,\beta,\nu}_{\xi,\alpha,\eta}\ {}^{IT}\langle[\mu][\beta][\nu]\rangle_i$ (red lines) estimated from the least square problem of Eq. (6) are compared with log $W(\xi, \alpha, \eta, i, IT)$ (circles), calculated from the MC simulation results using 10,000 samples for various combinations of the MH state (α, column) and the neighboring states (ξ and η, row). All results are from the MH_{18} (the central unit in the filament) in the left panel and from MH_5 (near the left end of MF) in the right panel, respectively, for *SL* = 2.2 μm.

[P] in response to the last four Ca peaks in Fig. 3, and the results were compared with those from the MC simulation at different *SL*s [1.9 and 2.2 μm (Fig. 6)]. In all MHs at both *SL*s, the ODE model and MC simulations correlated well. To clearly demonstrate the agreement, the absolute values of their differences were also shown (ERROR in Fig. 6).

Effects of SL on Twitch Duration

Using the same parameter set, we simulated a series of isometric twitches using both the MC simulation and the ODE model while varying the *SL* and compared the time courses with the experimental results reported by Janssen *et al.*[12] (Fig. 7). Because the Ca transient was not measured in Janssen's study, we applied the Ca transient shown in the bottom panel, and the force and [P] values were normalized by their peak values at $SL = 2.2$ μm. Both the MC simulation (Fig. 7a) and the ODE model (Fig. 7b) reproduced the experimental results reasonably well and clearly showed the *SL* dependence of twitch duration.

Simulations of Isometric and Shortening Twitches

Next, we applied a Ca transient reported in Janssen and de Tombe[11] to simulate a twitch under both isometric and shortening contraction (Fig. 8). Again we used the same parameter set, and the force and [P] values were normalized by the respective isometric peak values. For the simulation of a shortening twitch, we applied the time course of *SL*, and the interpolated parameter values were used for continuously changing *SL*s as described in the methods. Both the MC and ODE simulations successfully reproduced the experimental results ($R^2 = 0.987$ for MC and $R^2 = 0.982$ for ODE in the isometric contraction, and $R^2 = 0.988$ for MC and $R^2 = 0.977$ for ODE in the shortening contraction), however, to obtain the reasonable agreement, it was necessary to apply the Ca transient recorded under isometric condition to shortening twitch. The reason is not clear, but the use of [P] as the index of force and the absence of mechanisms regulating the affinity of Ca^{2+} to troponin C in the model may account for this contradictory result.

Effect of Cross-Bridge Kinetics on Force Relaxation

Finally, we examined the effect of cross-bridge kinetics on force relaxation by the MC and ODE simulations. For comparison, we adopted the results reported by Fitzsimons *et al.*[7] in which a stepwise reduction in the Ca^{2+} concentration was applied to skinned rat trabeculae composed of either 80%

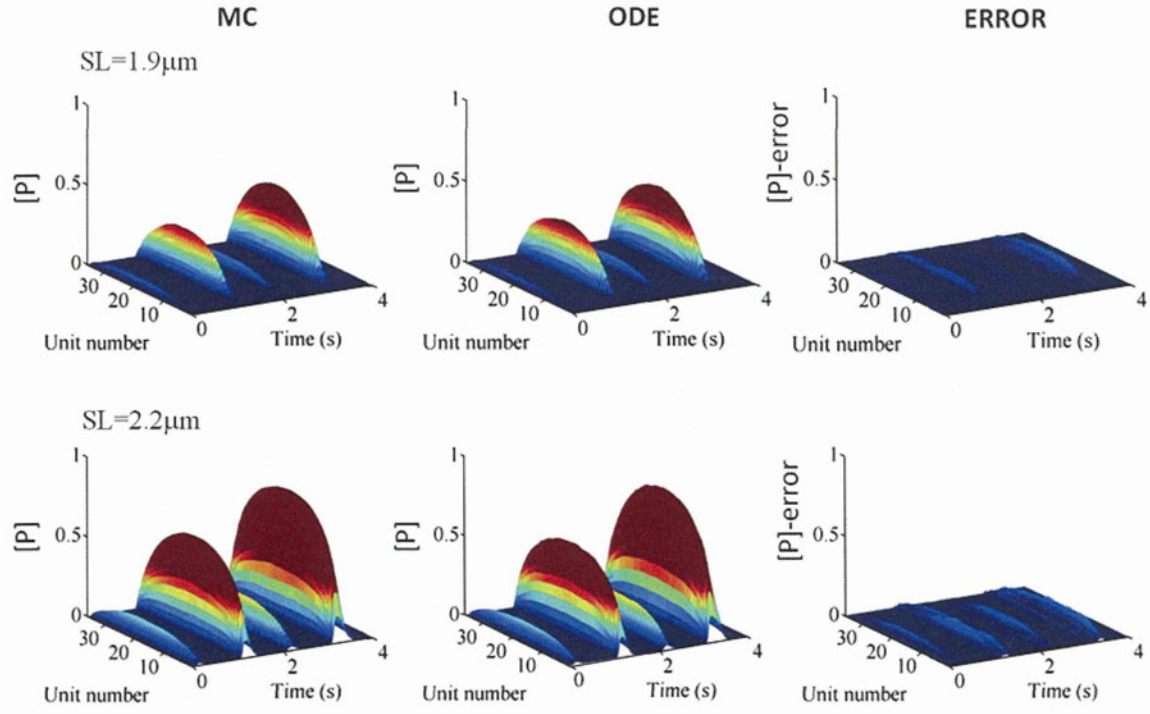

FIGURE 6. Comparisons between the ODE model and MC simulation at individual MHs. The fraction of bound cross-bridges [P] calculated using the ODE model (middle column) are compared with the MC simulation results (left column) while applying the Ca transients in Fig. 3. *SL* was set at 1.9 μm (top rows) or 2.2 μm (bottom rows). MC data are displayed as averaged values of 10,000 samples. The absolute values of the differences between the ODE and MC solutions are shown as ERROR (right column). The colors indicate the values (blue:0.0 red:0.3) of ratio (the fraction of bound cross-bridges [P]) (blue:0.0 red:0.3).

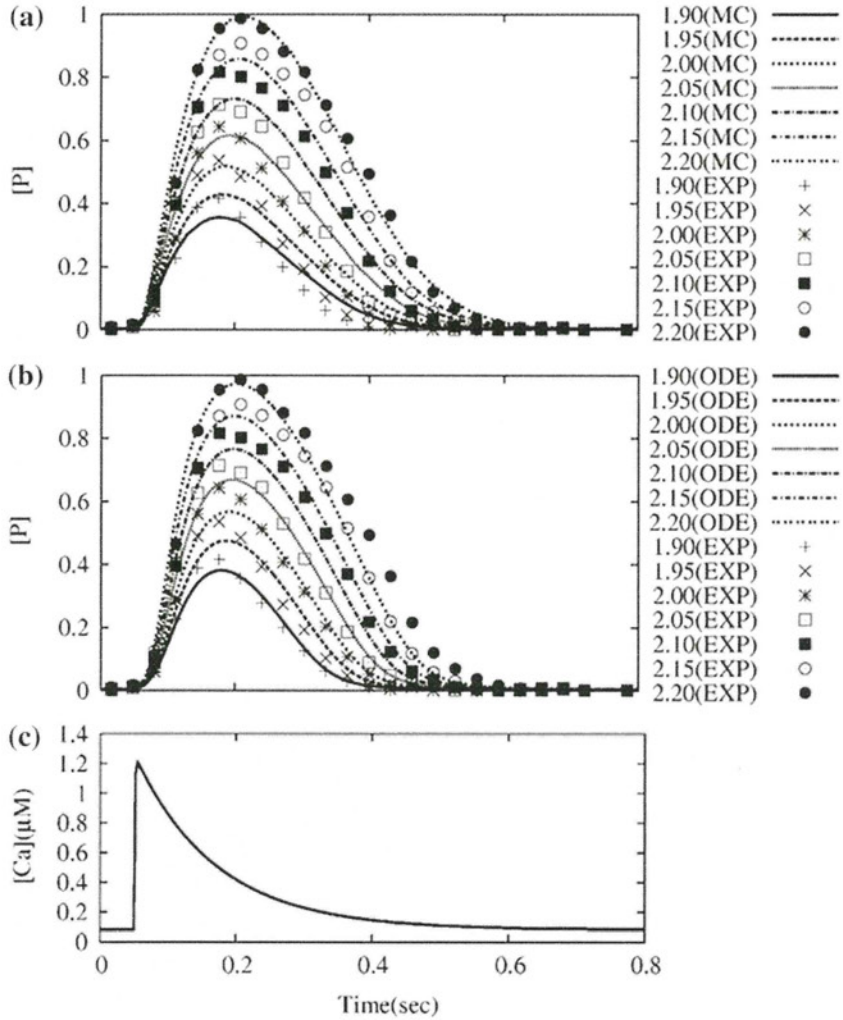

FIGURE 7. ***SL*** **dependence of twitch durations. Isometric twitches were compared while varying the *SL*. (a) Comparisons between the experiment (symbols) and MC simulation (lines); (b) comparisons between the experiment (symbols) and ODE (lines); (c) applied Ca transient.**

α-myosin heavy chain (control) or 100% β-myosin heavy chain (hypothyroid). We used the same parameter set for control and reduced the rate constant (K_{basic} 10 to 3 in Eq. (5)) for the hypothyroid case to replicate the slow cycling rate of a β-myosin heavy chain. To obtain agreement between the MC and ODE simulations ($R^2 = 0.976$), we used a memory length of 250 ms for the hypothyroid case. Both the MC and ODE simulations reproduced the exponential decline in [P] and the delay in force decline in the hypothyroid preparations that were observed in the experiment (Fig. 9). The half-times for relaxation (control vs. hypothyroid (ms)) were 80 and 152 (MC), and 72 and 117 (ODE) thus comparable to the experimental results (56 and 144) showing a 2-fold increase by hypothyroidism. Normalization of [P] by the initial value of the MC simulation made the initial ODE value greater than unity because of the differences in the numerical results between the two methods.

DISCUSSION

In this study, we propose an ODE model of the cardiac sarcomere dynamics with which we can approximate the results of MC simulation performed on the spatially detailed sarcomere model. By this approach, we reduced the huge computational cost usually required for MC simulations. Very recently, Campbell *et al.*[3] developed an ODE model similar to this model that describes nearest neighbor interactions. Their Markov model approach, without using approximation, theoretically gives us the accurate solution of the system, but the use of a ring configuration for the small number of regulatory units cannot reproduce the behavior of the units at the filament ends thus introducing errors. Additionally, the computational costs can become significant as the number of units approaches that of the actual thin filament. Furthermore, the ring simplification does not allow the

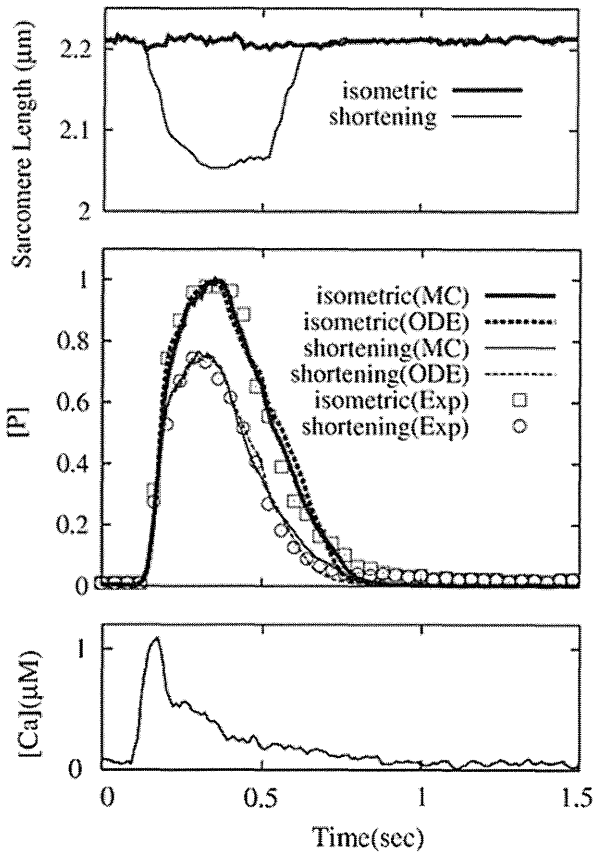

FIGURE 8. Model predictions of twitch contractions in response to experimentally observed Ca transient. Simulations were performed under isometric and shortening conditions. Ca transient (bottom panel) and length change (top panel) were digitized from the study by Janssen *et al.*[11] Calculated force ([P] values) was compared for isometric (case 1) and shortening (case 2) among the MC simulation (solid lines), ODE (dotted lines), and experimental results (symbols). [P] and force were normalized relative to the peak isometric values.

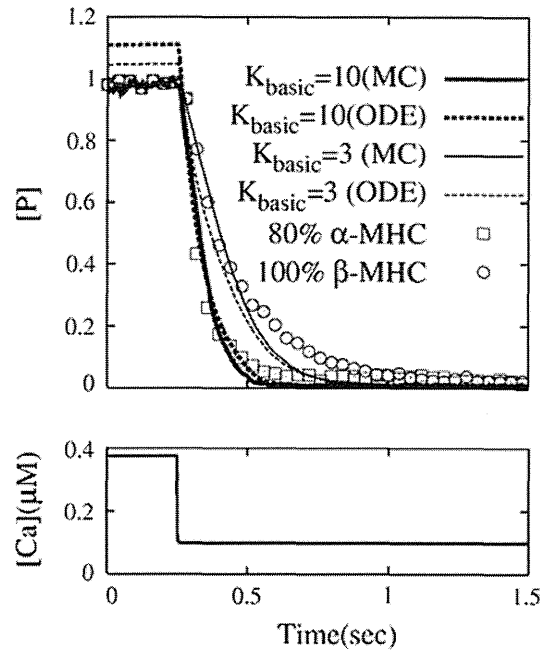

FIGURE 9. The effect of cross-bridge kinetics on the relaxation of force. We simulated experiments by Fitzsimons *et al.*,[7] in which a step reduction in Ca^{2+} concentration (bottom panel) was applied to the skinned muscle preparations in which myosin isoform composition was either 80% α-myosin heavy chain or 100% β-myosin heavy chain. Top panel shows the comparison for 80% α(experiment: square, MC: thick solid line, ODE: thick dotted line) and 100% β(experiment: circle, MC: thin solid line, ODE: thin dotted line).

simulation of *SL* change during the physiological contraction. Our ODE model with a realistic number of units in linear arrangement demonstrated good correlation with the MC simulation. Moreover, the results from our ODE model indicated that it can be applied to a wide range of cardiac physiology simulations.

Spatially-Detailed Sarcomere Model

The framework of the sarcomere model was adopted from the Ising model by Rice *et al.*[19] with modifications. First, to fit the fraction of bound cross-bridges–pCa curves (Fig. 4 upper panel), modulatory factors for Ca binding (χ_{RA}) and cross-bridge formation ($\chi_{RA} \cdot \chi_{LA}$) were multiplied by the transition rates. This modification also aided the reproducibility of the force–length relations.[6,17] Importantly, it was confirmed that in different sets of data, the predictive power of the ODE model is independent of the factors χ_{RA} and χ_{LA} indicating that the ODE model could accommodate the modifications made to it.

Mean Field ODE vs. Spatially-Detailed Models

To avoid the expensive MC simulations required for spatially detailed models of the sarcomere, various ODE models describing the average behavior of the regulatory unit have been reported,[13,15,20,21] but the problems and difficulties in the construction of such a mean field ODE model were pointed out in the literature.[18] Because cooperativity involves the interactions among the spatially arranged molecules, heterogeneous responses of the units are naturally expected and, in fact, the MC simulation studies reported heterogeneous activities of the units during activation.[10,22] Our MC simulation also revealed the heterogeneous activities of the units especially near the edge because these units lacking their neighbors on one side are destined to have small probability for making cross-bridges. The smaller probability of these edge units in turn affects the kinetics of the adjacent units to reduce their probabilities. In this manner, the edge effect is transmitted to the center of the filament, although progressively attenuated, to create the symmetrical

probability distribution as shown in Fig. 6. On the other hand, the probability distribution in this study (Fig. 6) is continuous thus making clear contrast to other spatial MC models, which show discrete "pockets" in probability distributions.[2,10] This difference was originated by our assumption of homogeneous binding probability along the thin filament which ignores the discrete distribution of myosin binding site and differences in their interval (pitch) from that of MHs. With the inclusion of these structural properties, our ODE model will be able to provide detailed information on the activity of each unit and the overall sarcomere without the added computational cost, which an ordinary mean-field approach can never attain.

Memory Length

In the ODE simulations, we introduced the memory length as the parameter for the estimation of the combinatory probability of the states. As expected from Eq. (20), the memory length should be comparable to the lifetime of each state, which in turn reflects the cycling rate of cross-bridges. In fact, for the simulation of different myosins (Fig. 9), we needed to adjust the memory length. Such an adjustment is needed for myosins with different levels of light chain phosphorylation.

Application of the Model

We applied our model to the contraction simulation under a wide range of conditions and compared the results with experimental reports. Under steady-state conditions, [P]–pCa relations showed a weak dependence of the Hill coefficient on *SL*, which is close to recent data obtained under precise *SL* control. In response to the dynamic Ca transients, the model successfully reproduced the *SL* dependence of twitch duration under isometric conditions as well. However, the salient feature of the present model is its applicability to the shortening contraction. Although the present application was limited to the case of prescribed length change, the incorporation of a viscoelastic element to the model will enable us to simulate the dynamic experiment with a dynamically changing afterload.

Limitation

Our ODE approximation method is based on the assumption that the combinatory state probabilities of three consecutive MHs can be represented as functions of the state probabilities of single units, but does not have any firm theoretical basis. Yet, the good predictive power in the simulation tests provides strong support to the validity of the model. However, we cannot be sure whether we can obtain similar results under other conditions. Further studies are needed. Finally, to evaluate accurately the generated force in heart muscle contraction simulations, we must further introduce viscoelastic effects to the units in P-states.

Future Directions

The development of an ODE model that approximates a spatially detailed model may open the possibility of the application of such models to a large scale model of circulation, such as the finite element model of the heart. However, the theoretical basis of the present ODE approximation remains to be elucidated.

APPENDIX

Determination of the Parameters from MC Simulation Results

The data obtained from the MC simulations of duration $[T_0{:}T_1]$ was divided into bins of equal time intervals (DT = 2.5 ms). Because updating in MC simulation was made every Δt = 2.5 μs, each bin was composed of 1000 data sets. In each updating step at each MH_i, the number of combinational states corresponding to $(\xi_{i-1}, \alpha_i, \eta_{i+1})$ were counted, where ξ_{i-1}, η_{i+1} = N or P and α_i = 0N, 1N, 1P, or 0P. Results were stored in a $2 \times 4 \times 2 \times nu \times NT$ sized array $cnt_{16}(\xi_{i-1}, \alpha_i, \eta_{i+1}, i, IT)$ for bin number $IT = 1,\ldots,NT (NT = T/DT)$ by using the following indexing: N = 1, P = 2 and 0N = 1, 1N = 2, 1P = 3, and 0P = 4. The above procedure was performed for the MC simulations repeated over 10,000 times for a single Ca condition (Fig. 3) to fill the array $cnt_{16}(\xi_{i-1}, \alpha_i, \eta_{i+1}, i, IT)$. The following arrays ($cnt_4$ and cnt_2) were generated from this data holding the number of individual state of the MH_i in bin IT.

$$cnt_4(\alpha,i,IT) = \sum_{\xi,\eta=\mathrm{N,P}} cnt_{16}(\xi,\alpha,\eta,i,IT)$$

$$cnt_2(\mu,i,IT) = \begin{cases} cnt_4(0\mathrm{N},i,IT) + cnt_4(1\mathrm{N},i,IT), & \text{if } \mu = \mathrm{N} \\ cnt_4(0\mathrm{P},i,IT) + cnt_4(1\mathrm{P},i,IT), & \text{if } \mu = \mathrm{P} \end{cases} \quad \text{(A1)}$$

Dividing the elements of these two arrays by the total number of data provides the estimate of probability. Therefore, we can obtain the following ratio that approaches the left-hand side in Eq. (21) as the number of samples increases.

$$W(\xi,\alpha,\eta,i,IT) = \frac{cnt_{16}(\xi,\alpha,\eta,i,IT)}{cnt_4(\alpha,i,IT)} \approx \frac{{}^t[\xi,\alpha,\eta]_i}{{}^t[\alpha]_i}, \quad \text{(A2)}$$

for $(IT - 1) \cdot DT \le t \le IT \cdot DT$.

Approximations of ${}^{t}\langle[\mu][\beta][\nu]\rangle_i$ can also be obtained from cnt_4 by applying the backward Euler time integration scheme to the ODE:

$$\frac{d}{dt}{}^{t}\langle[\mu][\beta][\nu]\rangle_i+\frac{1}{\tau}{}^{t}\langle[\mu][\beta][\nu]\rangle_i=\frac{1}{\tau}{}^{t}[\mu]_i{}^{t}[\beta]_i{}^{t}[\nu]_i,\ T_0<t\le T_1 \tag{A3}$$

that is fulfilled by ${}^{t}\langle[\mu][\beta][\nu]\rangle_i$ in Eq. (20) in the main text. This results in the following:

$${}^{IT+1}\langle[\mu][\beta][\nu]\rangle=\frac{1}{DT+\tau}\left(\tau\cdot{}^{IT}\langle[\mu][\beta][\nu]\rangle+DT\cdot\frac{mcnt(\mu,\beta,\nu,i,IT)}{(DT/\Delta t)^3\cdot MT^3}\right)$$

$$\text{with } mcnt(\mu,\beta,\nu,i,IT)=cnt_4(\mu,i,IT)cnt_4\times(\beta,i,IT)cnt_4(\nu,i,IT). \tag{A4}$$

Here, MT is the repeat number of MC simulations, and the interval index IT is identified with time $t = IT\cdot DT - T_0$.

The parameters $C(i)^{\mu,\beta,\nu}_{\xi,\alpha,\eta}$ were determined by minimizing the residual R in its logarithmic form as:

$$R(\xi,\alpha,\eta,i,IT)=\log W(\xi,\alpha,\eta,i,IT)-\sum_{\mu,\beta,\nu=0N,1N,1P,0P}C(i)^{\mu,\beta,\nu IT}_{\xi,\alpha,\eta}\langle[\mu][\beta][\nu]\rangle. \tag{A5}$$

In practice, we solved the following least-square problem for errors with weights of bias (cnt_{16}) on the log$W$ values derived from the larger number of samples assuming their reliability.

$$E(\xi,\alpha,\eta,i)=\sum_{IT=1}^{NT}\frac{cnt_{16}(\xi,\alpha,\eta,i,IT)}{MT}R(\xi,\alpha,\eta,i,IT)^2+\varepsilon\sum_{\mu,\beta,\nu}\left(C(i)^{\mu,\beta,\nu}_{\xi,\alpha,\eta}-\overline{C}\right)^2 \tag{A6}$$

Through this procedure, $W = 0$ is naturally eliminated in the error evaluation. The second term on the right-hand side of Eq. (A6) was added to avoid extraordinarily large values for the parameters $C(i)^{\mu,\beta,\nu}_{\xi,\alpha,\eta}$. In our simulations, $\varepsilon = 10^{-5}$ and $\overline{C} = -10$ were adopted.

The least square problem for the error E in Eq. (A6) results in the following system of linear equations with 64 unknowns $C(i)^{\bar\mu,\bar\beta,\bar\nu}_{\xi,\alpha,\eta}$ ($\bar\mu,\bar\beta,\bar\nu = 0N, 1N, 1P, 0P$).

$$\sum_{\bar\mu,\bar\beta,\bar\nu}\left(a^{\bar\mu,\bar\beta,\bar\nu}_{\mu,\beta,\nu}+\varepsilon\ \delta^{\bar\mu,\bar\beta,\bar\nu}_{\mu,\beta,\nu}\right)C(i)^{\bar\mu,\bar\beta,\bar\nu}_{\xi,\alpha,\eta}=b_{\mu,\beta,\nu},\quad \mu,\beta,\nu=0N,1N,1P\text{ or }0P \tag{A7}$$

Here, the coefficients in Eq. (A7) are given by

$$a^{\bar\mu,\bar\beta,\bar\nu}_{\mu,\beta,\nu}=\sum_{IT=1}^{NT}\frac{cnt_{16}(\xi,\alpha,\eta,i,IT)}{MT}{}^{IT}\langle[\mu][\beta][\nu]\rangle{}^{IT}\langle[\bar\mu][\bar\beta][\bar\nu]\rangle+\varepsilon,$$

$$b_{\mu,\beta,\nu}=\sum_{IT=1}^{NT}\frac{cnt_{16}(\xi,\alpha,\eta,i,IT)}{MT}{}^{IT}\langle[\mu][\beta][\nu]\rangle\times\log W(\xi,\alpha,\eta,i,IT)-\varepsilon\left(C(i)^{\mu,\beta,\nu}_{\xi,\alpha,\eta}-\overline{C}\right),$$

$$\delta^{\bar\mu,\bar\beta,\bar\nu}_{\mu,\beta,\nu}=\begin{cases}1, & \text{if } \bar\mu=\mu,\bar\beta=\beta,\bar\nu=\nu,\\ 0, & \text{otherwise.}\end{cases} \tag{A8}$$

Generation of test Ca transients

The last 4 Ca transients in Fig. 3 were generated by the following equation proposed by Rice *et al.*,[20] with the parameter set listed below.

$$[\mathrm{Ca}](t)=\begin{cases}\mathrm{Ca}_{\mathrm{diastolic}}\\ \left(\frac{\mathrm{Ca}_{\mathrm{amplitude}}-\mathrm{Ca}_{\mathrm{diastolic}}}{\beta}\right)\times\left(\exp\left(-\frac{t-t_{\mathrm{start}}}{\tau_1}\right)-\exp\left(\frac{t-t_{\mathrm{start}}}{\tau_2}\right)\right)+\mathrm{Ca}_{\mathrm{diastolic}}\end{cases} \tag{A9}$$

with

$$\beta=\left(\frac{\tau_1}{\tau_2}\right)^{-1/\left(\frac{\tau_1}{\tau_2}-1\right)}-\left(\frac{\tau_1}{\tau_2}\right)^{-1/\left(\frac{\tau_2}{\tau_1}-1\right)}. \tag{A10}$$

1st: $t_{\mathrm{start}} = 0.05\,\mathrm{s}$, $\mathrm{Ca}_{\mathrm{diastolic}} = 0.07\,\mu\mathrm{M}$, $\mathrm{Ca}_{\mathrm{amplitude}} = 1.4\,\mu\mathrm{M}$, $\tau_1 = 0.02\,\mathrm{s}$, $\tau_2 = 0.11\,\mathrm{s}$

2nd: $t_{\mathrm{start}} = 1.05\,\mathrm{s}$, $\mathrm{Ca}_{\mathrm{diastolic}} = 0.07\,\mu\mathrm{M}$, $\mathrm{Ca}_{\mathrm{amplitude}} = 2.8\,\mu\mathrm{M}$, $\tau_1 = 0.02\,\mathrm{s}$, $\tau_2 = 0.11\,\mathrm{s}$

3rd: $t_{start} = 2.05\,s$, $Ca_{diastolic} = 0.07\,\mu M$, $Ca_{amplitude} = 1.4\,\mu M$, $\tau_1 = 0.02\,s$, $\tau_2 = 0.14\,s$

4th: $t_{start} = 3.05\,s$, $Ca_{diastolic} = 0.07\,\mu M$, $Ca_{amplitude} = 2.8\,\mu M$, $\tau_1 = 0.02\,s$, $\tau_2 = 0.14\,s$

ACKNOWLEDGMENTS

This study was supported by the Japan Science and Technology Agency under the grant Collaborative Development of Innovative Seeds-Practicability Verification Stage, and the Japan Society for the Promotion of Science (JSPS) through its "Funding Program for World-Leading Innovative R&D on Science and Technology (FIRST Program)."

OPEN ACCESS

REFERENCES

[1]Campbell, K. Rate constant of muscle force redevelopment reflects cooperative activation as well as cross-bridge kinetics. *Biophys. J.* 72:254–262, 1997.

[2]Campbell, K. S. Filament compliance effects can explain tension overshoots during force development. *Biophys. J.* 91:4102–4109, 2006.

[3]Campbell, S. G., F. V. Lionetti, K. S. Campbell, and A. D. McCulloch. Coupling of adjacent tropomyosins enhances cross-bridge-mediated cooperative activation in a Markov model of the cardiac thin filament. *Biophys. J.* 98:2254–2264, 2010.

[4]Daniel, T. L., A. C. Trimble, and P. B. Chase. Compliant realignment of binding sites in muscle: transient behavior and mechanical tuning. *Biophys. J.* 74:1611–1621, 1998.

[5]Dobesh, D. P., J. P. Konhilas, and P. P. de Tombe. Cooperative activation in cardiac muscle: impact of sarcomere length. *Am. J. Physiol. Heart Circ. Physiol.* 282: H1055–H1062, 2002.

[6]Edman, K. A. Contractile properties of mouse single muscle fibers, a comparison with amphibian muscle fibers. *J. Exp. Biol.* 208:1905–1913, 2005.

[7]Fitzsimons, D. P., J. R. Patel, and R. L. Moss. Role of myosin heavy chain composition in kinetics of force development and relaxation in rat myocardium. *J. Physiol.* 15:171–183, 1998.

[8]Geeves, M., H. Griffiths, S. Mijailovich, and D. Smith. Cooperative [Ca^{2+}]-dependent regulation of the rate of myosin binding to actin: solution data and the tropomyosin chain model. *Biophys. J.* 100:2679–2687, 2011.

[9]Hunter, P. J., A. D. McCulloch, and H. E. D. J. ter Keurs. Modeling the mechanical properties of cardiac muscle. *Prog. Biophys. Mol. Biol.* 69:289–331, 1998.

[10]Hussan, J., P. P. de Tombe, and J. J. Rice. A spatially detailed myofilament model as a basis for large-scale biological simulations. *IBM J. Res. Dev.* 50:583–600, 2006.

[11]Janssen, P. M., and P. P. de Tombe. Uncontrolled sarcomere shortening increases intracellular Ca^{2+} transient in rat cardiac trabeculae. *Am. J. Physiol.* 272:H1892–H1897, 1997.

[12]Janssen, P. M., and W. C. Hunter. Force, not sarcomere length, correlates with prolongation of isosarcometric contraction. *Am. J. Physiol.* 269:H676–H685, 1995.

[13]Katsnelson, L. B., T. B. Sulman, O. E. Solovyova, and V. S. Markhasin. Cooperative mechanisms of thin filament activation and their contribution to the myocardial contractile function: assessment in a mathematical model. *Biophysics* 54:39–46, 2009.

[14]Kentish, J. C., H. E. D. J. ter Keurs, L. Ricciardi, J. J. J. Bucx, and M. I. M. Noble. Comparison between the sarcomere length–force relations of intact and skinned trabeculae from rat right ventricle: influence of calcium concentrations on these relations. *Circ. Res.* 58:755–768, 1986.

[15]Landesberg, A., and S. Sideman. Mechanical regulation of cardiac muscle by coupling calcium kinetics with cross-bridge cycling. *Am. J. Physiol.* 267:H779–H795, 1994.

[16]Mijailovich, S. M., J. J. Fredberg, and J. P. Butler. On the theory of muscle contraction: filament extensibility and the development of isometric force and stiffness. *Biophys. J.* 71:1475–1484, 1996.

[17]Rassier, D. E., B. R. Macintosh, and W. Herzog. Length dependence of active force production in skeletal muscle. *J. Appl. Physiol.* 86:1445–1457, 1999.

[18]Rice, J. J., and P. P. de Tombe. Approaches to modeling cross-bridges and calcium-dependent activation in cardiac muscle. *Prog. Biophys. Mol. Biol.* 85:179–195, 2004.

[19]Rice, J. J., G. Stolovitzky, Y. Tu, and P. P. de Tombe. Ising model of cardiac thin filament activation with nearest-neighbor cooperative interactions. *Biophys. J.* 84:897–909, 2003.

[20]Rice, J. J., F. Wang, D. M. Bers, and P. P. de Tombe. Approximate model of cooperative activation and cross-bridge cycling in cardiac muscle using ordinary differential equations. *Biophys. J.* 95:2368–2390, 2008.

[21]Rice, J. J., R. L. Winslow, and W. C. Hunter. Comparison of putative cooperative mechanisms in cardiac muscle: length dependence and dynamic responses. *Am. J. Physiol. Heart Circ. Physiol.* 276:1734–1754, 1999.

[22]Zou, G., and G. N. Phillips, Jr. A cellular automaton model for the regulatory behavior of muscle thin filaments. *Biophys. J.* 67:11–28, 1994.

Journal of Biomechanics 45 (2012) 815–823

Contents lists available at SciVerse ScienceDirect

Journal of Biomechanics

journal homepage: www.elsevier.com/locate/jbiomech
www.JBiomech.com

Critical role of cardiac t-tubule system for the maintenance of contractile function revealed by a 3D integrated model of cardiomyocytes

Asuka Hatano, Jun-ichi Okada, Toshiaki Hisada, Seiryo Sugiura *

Graduate School of Frontier Sciences, The University of Tokyo, 5-1-5 Kashiwanoha, Kashiwa, Chiba 277-8581, Japan

ARTICLE INFO

Article history:
Accepted 30 September 2011

Keywords:
Excitation–contraction coupling
Subcellular structure
t-tubule
Reaction–diffusion
Finite element methods

ABSTRACT

T-tubules in mammalian ventricular myocytes constitute an elaborate system for coupling membrane depolarization with intracellular Ca^{2+} signaling to control cardiac contraction. Deletion of t-tubules (detubulation) has been reported in heart diseases, although the complex nature of the cardiac excitation–contraction (E–C) coupling process makes it difficult to experimentally establish causal relationships between detubulation and cardiac dysfunction. Alternatively, numerical simulations incorporating the t-tubule system have been proposed to elucidate its functional role. However, the majority of models treat the subcellular spaces as lumped compartments, and are thus unable to dissect the impact of morphological changes in t-tubules. We developed a 3D finite element model of cardiomyocytes in which subcellular components including t-tubules, myofibrils, sarcoplasmic reticulum, and mitochondria were modeled and realistically arranged. Based on this framework, physiological E–C coupling was simulated by simultaneously solving the reaction-diffusion equation and the mechanical equilibrium for the mathematical models of electrophysiology and contraction distributed among these subcellular components. We then examined the effect of detubulation in this model by comparing with and without the t-tubule system. This model reproduced the Ca^{2+} transients and contraction observed in experimental studies, including the response to beta-adrenergic stimulation, and provided detailed information beyond the limits of experimental approaches. In particular, the analysis of sarcomere dynamics revealed that the asynchronous contraction caused by a large detubulated region can lead to impairment of myocyte contractile efficiency. These data clearly demonstrate the importance of the t-tubule system for the maintenance of contractile function.

1. Introduction

In mammalian ventricular myocytes, the cell membrane (sarcolemma) invaginates to the cell interior at a regular interval to form the well-organized transverse (t-) tubule system. As voltage-operated L-type Ca^{2+}-channels are clustered in the t-tubules where they face the junctional part of the sarcoplasmic reticulum (SR) in close proximity, the t-tubule system is believed to play a crucial role in coupling the depolarization signal with Ca^{2+}-release from the SR (Brette and Orchard, 2003). In fact, atrial myocytes with a poorly-developed t-tubule system exhibit slow propagation of the Ca^{2+} signal from the periphery to the center of the cell (Kirk et al., 2003). Further, experimental deletion of t-tubules (detubulation) in ventricular myocytes by osmotic expansion (Brette et al., 2002; Kawai et al., 1999) or long term culture (Louch et al., 2004) results in an asynchronous rise in intracellular Ca^{2+} concentration $[Ca^{2+}]$ upon electrical stimulation as in pathological deletion (Dibb et al., 2009; Heinzel et al., 2008). Nevertheless, the causal relationship between t-tubule structure, $[Ca^{2+}]$ dyssynchrony, and contractile dysfunction of the myocytes often observed in diseased hearts remains unclear. For instance, structural remodeling of the t-tubule system is not only observed in the advanced stage of heart failure (Song et al., 2006), but it can occasionally start early in the compensated stage of hypertrophied hearts without contractile dysfunction (Wei et al., 2010). Remodeling includes the t-tubular disarray observed in mechanically unloaded myocytes, in which abnormal Ca^{2+} release is observed without appreciable changes in action potential and density of t-tubules as estimated from membrane fluorescence (Ibrahim et al., 2010). Furthermore, t-tubule alteration is not always observed in heart failure, while the localized drop out in excitation–contraction coupling (ECC) efficacy apparently caused by t-tubule remodeling can be explained by the altered action potential waveform characterized by the reduced transient outward current (Bers, 2006; Harris et al., 2005).

An alternative approach to study the functional impact of t-tubules is numerical simulation, with which we can perform *in silico* experiments under totally controlled conditions. The crucial

* Corresponding author. Tel.: +81 3 5841 8393; fax: +81 3 5841 6376.
E-mail address: sugiura@k.u-tokyo.ac.jp (S. Sugiura).

0021-9290/$ - see front matter © 2011 Elsevier Ltd. All rights reserved.
doi:10.1016/j.jbiomech.2011.11.022

part of the modeling of cardiac myocytes is the representation of the calcium-induced calcium release (CICR) mechanism. Until recently, the majority of studies used the 'common pool model' (Stern, 1992) in which all Ca^{2+} currents are mediated by the L-type Ca^{2+} channel (LCC) and the release flux from the SR flow into a common compartment, and the Ca^{2+} concentration in this compartment controls the activity of the SR Ca^{2+} release channel (ryanodine receptor: RyR). However, as this modeling strategy cannot reproduce the graded Ca^{2+} release, alternative formulations have been devised. For example, Greenstein et al. (2006) proposed a local control model in which simulated the gating of individual LCCs and RyRs in dyadic space to successfully reproduce the graded Ca^{2+} release. Nevertheless, both modeling approaches treat the subcellular spaces as a lumped compartment and ignore geometrical factors, and as such are unsuitable for examining the effect of structural changes in t-tubules. Three-dimensional (3D) models of cardiac myocytes studying the impact of 3D t-tubules on electrophysiology and 3D Ca^{2+} dynamics have also been reported (Cheng et al., 2010; Lukyanenko et al., 2009; Yu et al., 2011). However, although these models reproduce either a simple or realistic shape of t-tubule structure, other subcellular components are not explicitly modeled and the diffusion of Ca^{2+} is calculated in the homogeneous cytosolic space assuming a uniform distribution of troponin C throughout the cytosol.

Thus, as yet there are no simulation models that integrate the electrophysiology and contraction in a detailed 3D structure to examine the functional impact of t-tubule structure in health and diseased states. In the present study, we extended our previous system (Okada et al., 2005) to develop a finite element model of cardiomyocyte integrating electrophysiology, Ca^{2+} dynamics, and contractile process with detailed subcellular structures to evaluate the impact of the spatial arrangement of t-tubules in the signal transduction involved in ECC. The simulation results reproduced both the propagation of Ca^{2+} signals and the contractile behavior for both normal and detubulated myocytes previously reported in experimental studies. Furthermore, the detailed information provided on Ca^{2+} concentration, stress, and sarcomere strain beyond the limit of experimental approach demonstrated not only the importance of t-tubules in contractile function but also the utility of this model for studying cardiac mechanics.

2. Methods

2.1. 3D finite element model of the myocyte

The structure of the 3D finite element model of myocytes is shown in Fig. 1C–E. Ion channels, pumps, and exchangers are distributed in surface sarcolemma and t-tubules with specific densities, as previously reported for guinea pig ventricular myocyte (Pasek et al., 2008). Mitochondria were modeled as a Ca^{2+} sink, although energy metabolism was not incorporated in this study. To reduce computational costs the segment containing three myofibrils of one sarcomere length was modeled together with the adjacent cell membrane and organelle (2816 nodes and 2107 elements). The rationale behind this modeling strategy was the longitudinal periodicity and axial symmetry of the myocyte. Subcellular components including the mitochondria, myofibril (A-zone, I-zone, and M-line), junctional and network sarcoplasmic reticulum (JSR and NSR respectively), cell membrane, and t-tubules were located at the appropriate nodes to reproduce the anatomical structure and occupy the relative volume (Aliev et al., 2002; Bers, 2001; Chen-Izu et al., 2006; Cortassa et al., 2006). The function of each subcellular component was primarily based

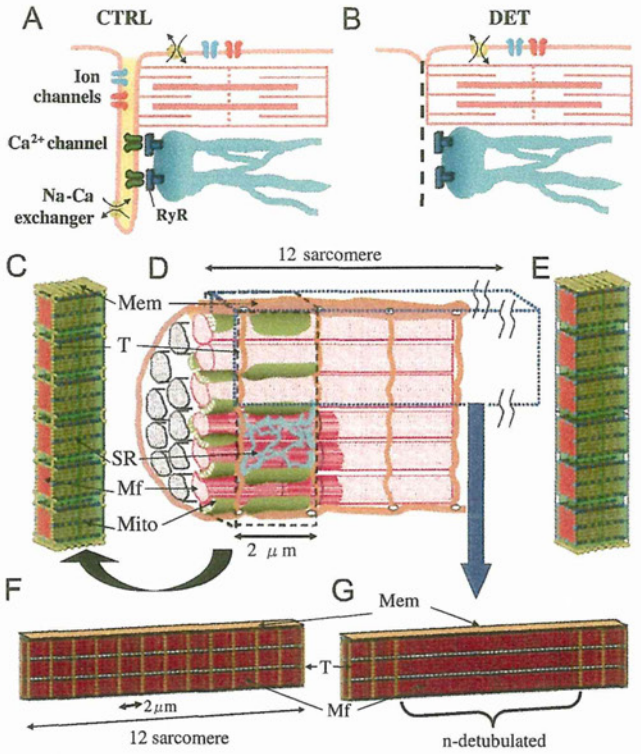

Fig. 1. (A) Control model (CTRL) with normal t-tubule structure. (B) Detubulated model (DET) with orphan ryanodine receptor. (C–E) Schematic diagram of the 3D cardiomyocyte model. (D) Six myofibrils of one sarcomere length were modeled in finite element mesh with subcellular structures (C, CTRL; E, DET). Ion channels and exchangers are distributed over the t-tubules and sarcolemma. Mem: sarcolemma, Mf: myofibril, Mito: mitochondria, SR: sarcoplasmic reticulum, T: t-tubule. (F) Twelve sarcomere mesh with normal t-tubule structure. (G) Twelve sarcomere mesh with t-tubule deleted in the mid n-sarcomeres.

on the previously proposed mathematical formulation for guinea pig ventricular cardiomyocyte (Cortassa et al., 2006). Additionally, to investigate the effect of regional disorganization of the t-tubule system, we created larger models consisting of three myofibrils of 12-sarcomere length (Fig. 1F and G). In these cases, to save the computational cost, coarse meshes were used and half of the model (6 sarcomere length) was calculated considering its symmetry. The model consisted of 4340 nodes and 3420 elements. The reaction–diffusion fields for Ca^{2+} were defined in the cytosolic space, as follows:

$$\frac{d[Ca^{2+}]_i}{dt} = \nabla\cdot(\mathbf{D}\nabla[Ca^{2+}]_i) + f_i([Ca^{2+}]_i) \quad (1)$$

where $\mathbf{D}$ describes the diffusivity of Ca^{2+}, $[Ca^{2+}]_i$ is the concentration of Ca^{2+} at position i, and $f_i([Ca^{2+}]_i)$ is the function describing the reaction of Ca^{2+} which corresponds to elementary processes of each subcellular components including mitochondria, JSR and so on, and which was defined appropriately for each node to reproduce the anatomical structure.

The diffusion coefficient for the longitudinal direction was estimated from an *in vitro* experiment (de Graaf et al., 2000) and set at D^{Ca}=0.3, ($\mu m^2/ms$). With regard to the coefficient in the transverse direction, we multiplied this value by 0.6265 based on *in vivo* cardiac myofibril results (Vendelin and Birkedal, 2008). Every node on the membrane and t-tubule permeates ions according to the local ion concentration and shares a membrane potential. As experimental data suggested that the whole cell membrane is electrically well coupled (Orchard and Brette, 2008), the membrane potential was treated as uniform throughout the

model. Ion channel distributions on peripheral and t-tubule membrane were defined as previously reported (Pasek et al., 2008) (see Supplemental Table 2). At the Ca^{2+} release site the channel distribution is different from other regions of the t-tubule membrane, and only the L-type Ca^{2+} channel (LCC) is clustered without other ion channels. Here, the LCC, JSR, subspace, and the local cytosolic space share a common node, but possess their own Ca^{2+} concentrations for finite element analysis. Upon depolarization of the membrane potential triggered by stimulation current, LCC opens and the Ca^{2+} current through the LCC (I_{Ca}) flows into the subspace and activates ryanodine receptors (RyR) located on the JSR. This triggers Ca^{2+} release from the JSR (J_{rel}) into the subspace, and the released Ca^{2+} moves to the cytosolic node to diffuse throughout the entire cytosol. Within the cytosolic space, Ca^{2+} is either taken up by the Ca^{2+} uniporter of the mitochondrial node, bound to troponin C on the thin filament, or is sequestered by Ca^{2+} pump (SERCA2) on the NSR, before eventually being transported back to the JSR. Further details outlining the model can be found in Supplementary Material.

The contraction model developed by Negroni and Lascano (1996) was located at each point of the A-zone and generated force depending on the local Ca^{2+} concentrations and sarcomere length. Using these force values as boundary conditions, the following mechanical equilibrium (2) and compressibility control condition (3) on variables ($\mathbf{u}$, λ) were solved using the finite element method:

$$\int_V \left(2\frac{\partial W}{\partial \mathbf{C}} + \lambda J\mathbf{C}^{-1}\right) : \delta\mathbf{E}dV + \int_{S_t} \tilde{\mathbf{t}}_b \cdot \delta\mathbf{u}dS = 0 \quad (2)$$

$$\int \delta\lambda\left(J-1-\frac{2\lambda}{\kappa}\right)dV = 0 \quad (3)$$

where $\mathbf{u}$ is displacement, W is strain energy potential, $\mathbf{C}$ is right Cauchy–Green deformation tensor, $\mathbf{E}$ is Green–Lagrange strain tensor, J is the square root of the determinant of $\mathbf{C}$, V is analysis volume, λ is a Lagrange multiplier corresponding to $-1/2$ of the pressure, κ is bulk modulus, $\tilde{\mathbf{t}}_b$ is the stress boundary condition calculated from A-zone force generation, and S_t is the surface where stress boundary condition is defined.

The cell was assumed as nearly incompressible hyperelastic material, with anisotropic constitutive equations for myofibril and isotropic constitutive equations of Mooney–Rivlin material for the other spaces previously reported (Okada et al., 2005). Full details of the mathematical modeling can be found online in Supplementary Material.

2.2. Detubulated myocyte models

The detubulated model (DET) was created by removing the t-tubules from the control model (CTRL) (Fig. 1A) along with the Ca^{2+} channels, Na^{+}–Ca^{2+} exchangers, and other channels distributed in it. As a result, the Ca^{2+} release channels (RyR) on the SR were left as orphan RyR (Fig. 1B). To analyze the effect of regional disorganization of the t-tubule system, we created two regionally detubulated models with either a large (8 sarcomere-length: DET8) or small (4 sarcomere-length: DET4) detubulated region, and compared them with the non-detubulated control myocyte model (Fig. 1F and G). We also compared the models in which half of the t-tubules were removed homogeneously (every other transverse tubule was deleted: homogenous model) or by deletion of the middle six t-tubules as a cluster (clustered model).

2.3. Simulating the adrenergic stimulation

In CTRL and DET models, the influences of adrenergic stimulation were simulated by up-regulation of L-type Ca^{2+} channel current by 50%, lowering the threshold $[Ca^{2+}]$ level for Ca^{2+} release from RyR by 20%, and tripling the maximum velocity of SR Ca^{2+} pump, as previously reported (Brette et al., 2005, 2004). We also simulated a case in which only the L-type Ca^{2+} current was up-regulated (Harris et al., 2005).

2.4. Computation

All the program codes (including solver and finite element integration) were written in-house using Fortran language, and the computation was performed using an Intel Xeon CPU (3.2 GHz).

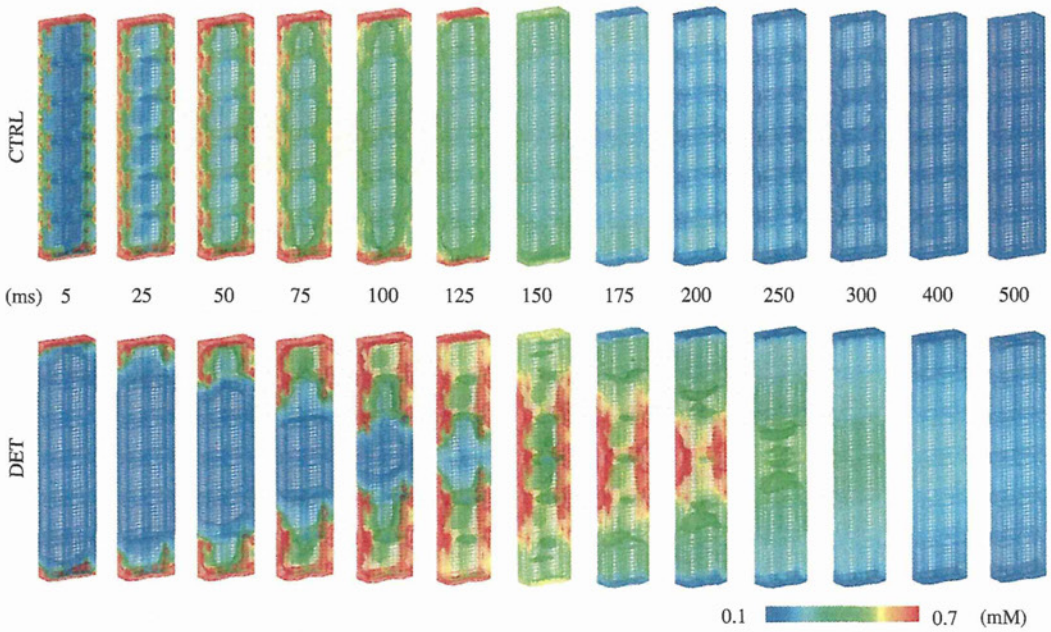

Fig. 2. Time lapse images of Ca^{2+} propagation in control (CTRL) and detubulated (DET) myocyte models under unloaded conditions. Ca^{2+} concentrations in the laterally arranged six sarcomeres are shown in color-coding indicated below. The numbers in the middle indicates the time (msec) after the stimulation.

3. Results

3.1. Ca^{2+} propagation and contraction in detubulated myocyte

The Ca^{2+} propagation and unloaded contraction of control and detubulated myocyte models in time-lapse images are shown in Fig. 2 (see also Supplemental Movie 1). In CTRL, $[Ca^{2+}]$ increased simultaneously at the surface membrane and Ca^{2+} release sites distributed along the t-tubules, and rapidly propagated towards the A-line region. Consequently, all the sarcomeres in the model contracted synchronously. By contrast, $[Ca^{2+}]$ in DET was initiated only at the surface membrane and propagated slowly to the center of the cell, resulting in slow and asynchronous contraction.

Supplementary material related to this article can be found online at doi:10.1016/j.jbiomech.2011.11.022.

Next, for comparison with the experimentally observed transverse line scan using confocal microscopy, we simulated isometric contraction, and sampled and plotted the $[Ca^{2+}]$ on the line running transversely along the t-tubules after the onset of excitation, as well as the local Ca^{2+} transients sampled at the sub-sarcolemma (SS) and core (CC) regions (Fig. 3A and B). The regularly spaced bright spots in these figures correspond to the Ca^{2+} release sites. There was a significant delay in local Ca^{2+} transients in the core region of DET compared with CTRL, and both the time to peak and the end of the whole-cell Ca^{2+} transient, averaged over the entire region, was significantly delayed compared with CTRL (black lines in the bottom panels). The propagation velocity of Ca^{2+} transients was 31 μm/s, comparable to those observed experimentally (48.4 ± 5.2 μm/s; Yang et al. (2002)). Upon adrenergic stimulation, the amplitude of the Ca^{2+} transient increased and its duration decreased in CTRL (Fig. 3C). In the detubulated myocyte the lag between the periphery and the core was reduced (Fig. 3D), such that the whole-cell Ca^{2+} transient resembled that of the control (blue lines in the bottom panels). For validation, we compared these results with the

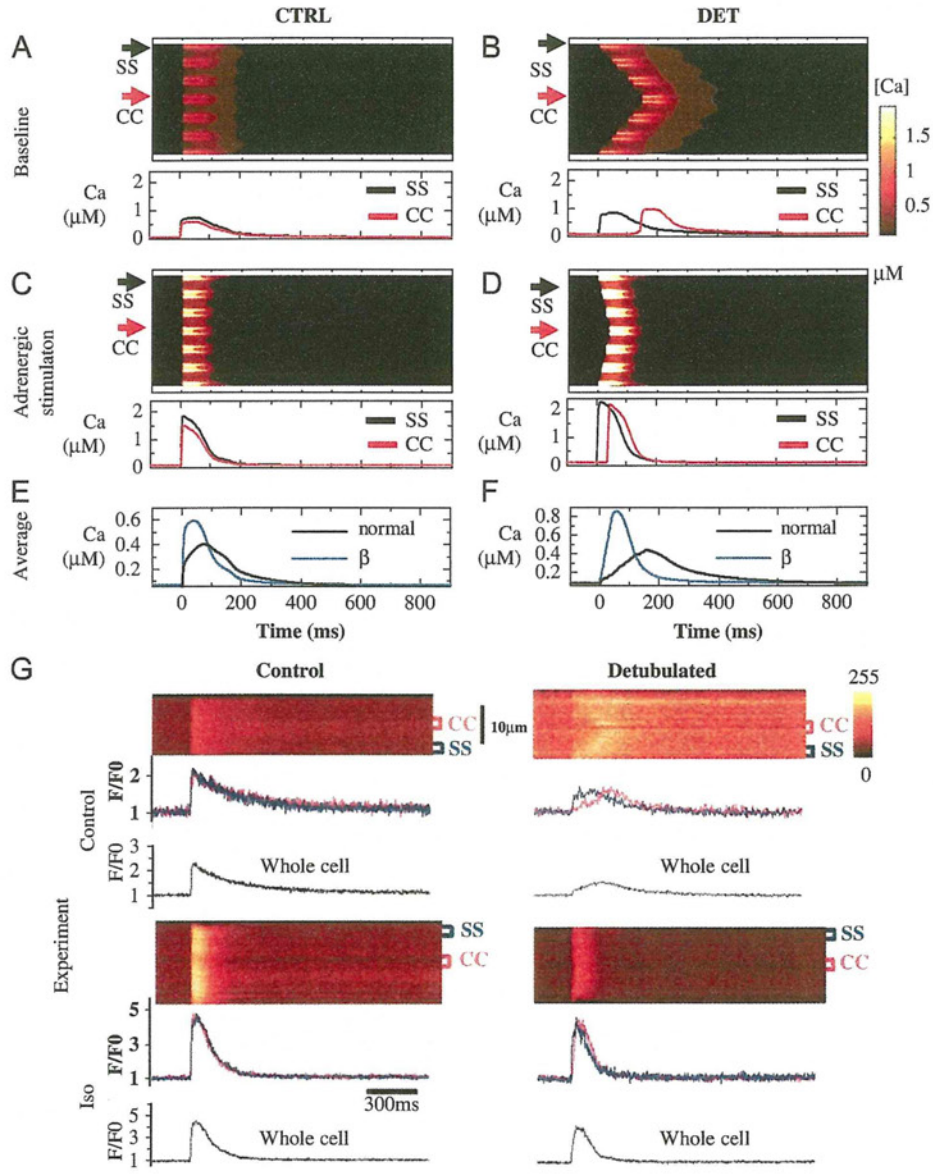

Fig. 3. Simulated transverse line scans of control (CTRL) model (A and C) and detubulated (DET) model (B and D) under control conditions (A and B) and under beta adrenergic stimulation (C and D) of isometric contraction. Each panel shows a line scan image of Ca^{2+}. concentration with time courses of the local Ca^{2+} concentration sampled at the CC and SS (attached below). The bottom panels compare the whole cell averaged Ca^{2+} transients of A *vs.* C (in E) and B *vs.* D (in F). G) Experimental data of line scans and traces of local and averaged Ca^{2+} transients from Brette et al. (2004) are provided for comparison by copyright permission of Elsevier.

experimental observations of Brett et al. (2004) (Fig. 3G). Our simulation model reproduced the effect of detubulation under both baseline and adrenergic stimulation. On the other hand, when only the I_{Ca} was up-regulated, the re-synchronization effect was minimal and a significant delay in the local Ca^{2+} transient in the cell center remained. Propagations in the DET model under baseline (without adrenergic stimulation), up-regulation of I_{Ca}, and β-adrenergic stimulation are shown in Fig. 4. For baseline, I_{Ca} up-regulation, and β-adrenergic stimulation, propagation times were 150, 115, and 35 ms, respectively, and propagation velocities were 31, 40, and 133 μm/sec, respectively.

We also examined the role of Na^+–Ca^{2+} exchanger (NCX) current distributed in t-tubules (Pasek et al., 2008) by comparing the averaged Ca^{2+} transients (Fig. 5A), L-type Ca^{2+} channel (Fig. 5B), and NCX (Fig. 5C) currents between the CTRL and the DET models. The total amounts flowing in and out of the model were compared for the currents. While the Ca^{2+} transient of the CTRL model exhibited a sharp rise triggered by the L-type Ca^{2+} channel current, the transient of the DET model triggered by diffuse Ca^{2+} increased slowly to its peak. After the peak, the Ca^{2+} transient of the DET model remained elevated. In the DET model, both the L-type Ca^{2+} channel current and the NCX current were significantly decreased compared with the control model, reflecting the localization of these currents in the t-tubules. These differences in currents contributed to the slow decay in the DET model, although the decay phase of the Ca^{2+} transient was dominated by the SR Ca^{2+} pump for both the CTRL and DET models.

3.2. *Propagation of Ca^{2+} is influenced by the contraction mode*

Next, we compared transverse line scans of the Ca^{2+} signals under different loading conditions (Fig. 6). For the isotonic contraction, afterload was set at 25% of the maximum isometric force. As the afterload was reduced (A: isometric→B: isotonic→C: unloaded), shortening of the myocyte increased the cell width. Although the initial propagation speed was similar (~30 μm/s), the resultant widening of the space between the adjacent Ca^{2+} release sites caused a progressive delay in Ca^{2+} propagation (~20 μm/s), and the propagation was finally terminated under the unloaded condition (Fig. 6C). A similar phenomenon was reported in the experimental study by Yang et al. (2002) (Fig. 6D).

3.3. *Regional loss of t-tubules*

The effects of regional detubulation on Ca^{2+} transient and contraction were examined using the 12-sarcomere model under isometric conditions (Fig. 7A). In contrast to the control myocyte showing synchronized Ca^{2+} transient and contraction, slow propagation of Ca^{2+} in the detubulated region progressively delayed the completion of contraction as the detubulated region became increased (Fig. 7A and Supplemental Movie 2). The amplitude and timing of the peak isometric force were also decreased and delayed, respectively, depending on the size of the detubulated region (Fig. 7B). To further analyze the contractile dysfunction of the detubulated myocyte, we examined the Ca^{2+} transient, sarcomere length, and developed force at each sarcomere (Fig. 8). The presentation mimicking the longitudinal line scan mode clearly demonstrated a progressive delay of Ca^{2+} propagation toward the center of the detubulated region (Fig. 8 top panels). Although the total muscle length was made isometric, asynchrony of the local Ca^{2+} transient in the detubulated models induced the internal shortening of the early-activated sarcomere and lengthening of the resting sarcomere (Fig. 8, middle panels). In particular, the large internal shortening observed in the DET8 model with the large detubulated region is the likely cause of the greater depression in initial rise of isometric force (Fig. 7B), via inhibition of development of force locally (Fig. 8 bottom panels). To investigate the effect of the size of individual detubulation, we also compared the homogeneous model and the clustered model that both had the same number of t-tubules. The homogeneous model showed no variation in sarcomere length, and the force developed smoothly, similar to the control myocyte without detubulation (Fig. 9). Internal shortening in the clustered model caused the depression of force development in the initial phase (Fig. 7C), and may also have induced a deleterious effect. In addition, although energy metabolism was not considered in this simulation, internal shortening is expected to reduce the contractile efficiency by wasting energy according to the Fenn effect.

Supplementary material related to this article can be found online at doi:10.1016/j.jbiomech.2011.11.022.

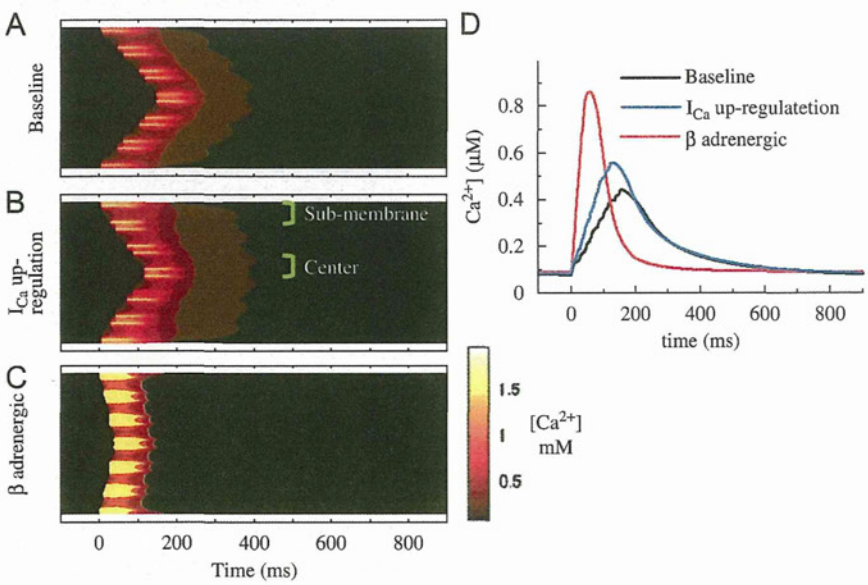

Fig. 4. Simulated transverse line scans and averaged Ca^{2+} transients of the detubulated model during the isometric contraction under baseline (A and D, black line), I_{Ca} up-regulation (B and D, blue line), and β-adrenergic (C and D, red line) conditions.

4. Discussion

4.1. 3D model of cardiomyocyte

In the present study, we extended our previous 3D cardiomyocyte model to incorporate ion currents distributed heterogeneously in the surface membrane and the t-tubule system to examine the impact of the t-tubule system on cardiac function. We adopted the sarcomere model of Negroni and Lascano (1996) for cardiac contraction. Although this simple model is not capable of reproducing the cooperative activation of actin-myosin interactions, we previously reported its robustness and compatibility with the FEM model (Okada et al., 2005; Watanabe et al., 2004). These complex models can reproduce various phenomena including cooperativity, quick-stretch, and release, but may require significant computational cost. The models of electrical activity by Cortassa et al. (2006) do not differ significantly from the model by Rudy (Livshitz and Rudy, 2007), but allow us to extend the model to include metabolic processes in future studies. However, as this model is a lumped parameter model, the distributions of ion channels in the t-tubule system and the volume fraction of the sub-compartments require adjustment for the current 3D model.

In the detubulated model, Ca^{2+} transients initiated at the peripheral membrane by depolarization propagate to the center of the cell slowly by a series of reaction diffusion processes (CICR). As a result, the Ca^{2+} transient averaged over the entire region showed a delay in time to peak and a slow decay. Slow decay was also observed in local Ca^{2+} transients due to the loss of t-tubular Na-Ca exchange current, as suggested experimentally (Kawai et al., 1999; Pasek et al., 2008; Yang et al., 2002). In addition, under adrenergic stimulation, the detubulated model showed faster Ca^{2+} propagation and the synchronization of the Ca^{2+} transient was restored. The lower threshold $[Ca^{2+}]$ level for Ca^{2+} release and the larger Ca^{2+} release flux through up-regulation of LCC and SR (up-regulation of SR Ca^{2+} pump resulted in higher content and larger release) accelerated the CICR and the reaction–diffusion processes. This synchronizing effect of beta adrenergic stimulation on detubulated cells was also observed in experimental studies (Brette et al., 2004; Smyrnias et al., 2010). In contrast to our simulation results, Harris et al. (2005) was able to recover synchronous Ca^{2+} release in failing feline myocytes only by increasing I_{Ca} induced by the normalization of action potential. However, although the authors did not examine the t-tubule morphology in their failing myocytes, they show a spotty Ca^{2+} release pattern suggesting that a large area of couplon loss did not take place in their preparations. Considering our simulation result with the small detubulated region (DET4 or homogeneous model), we speculate that if the area of detubulation is small, only the increase in I_{Ca} could allow recovery of the normal cardiomyocyte E–C coupling function, while if the area of detubulated is large, the recovery may not be possible even with multiple compensatory mechanisms.

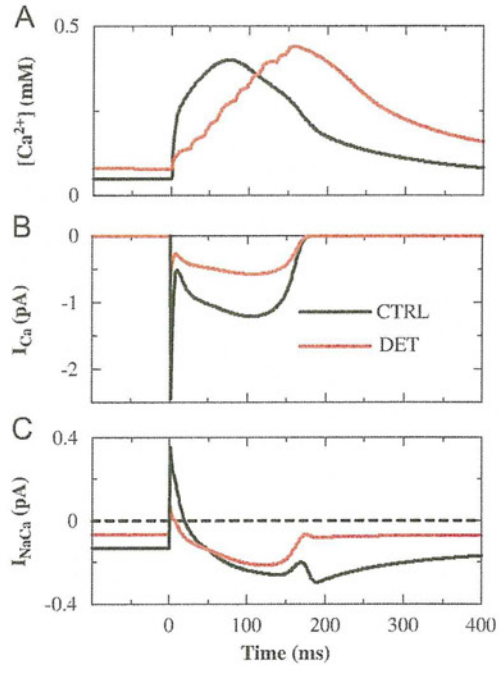

Fig. 5. Ca^{2+} transients and currents in CTRL (black line) and DET (red line) models under isometric condition. (A) Ca^{2+} transients averaged over the sarcomere. (B) L-type Ca^{2+} channel current. (C) Na^{+}–Ca^{2+} exchanger current.

4.2. Impact of t-tubule disorganization on cardiac dysfunction of the diseased heart

In cardiomyocytes isolated from diseased hearts, t-tubules are lost heterogeneously and the area of disorganization increases progressively (Cannell et al., 2006; Heinzel et al., 2008; Louch

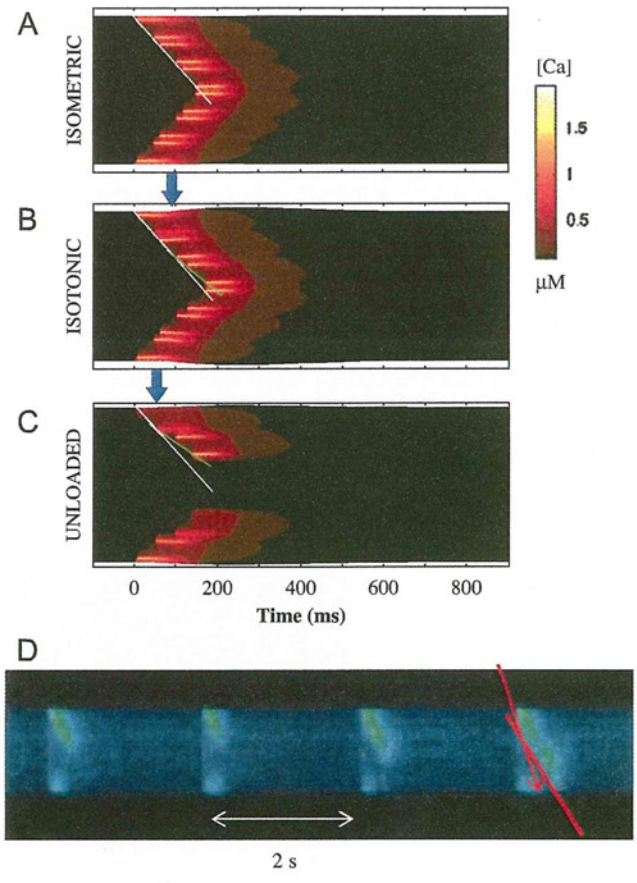

Fig. 6. Transverse line-scan images of detubulated (DET) model under different contraction modes. (A) Isometric contraction. (B) Isotonic contraction. (C) Unloaded contraction. While a single tangential line (white line) was well fit to the Ca^{2+} propagation in A, additional lines (green) were required in B and C due to the reduction of propagation velocity in the core region. Propagation velocity calculated from the slope of the tangential lines were similar in all cases at the initial part (white line: 31 μm/s), but decreased in B (21 μm/s) and C (18 μm/s), both calculated from the slope of the green lines. Blue arrows indicate the initiation of widening. (D) Experimental transverse line-scan image of detubulated myocyte demonstrating incomplete propagation of Ca^{2+}. Two tangential lines were fit, similar to above (reproduced from Yang et al. (2002) by copyright permission of the American Heart Association).

et al., 2004,2006). Our simulation revealed a clear dependence of cardiac dysfunction on the area of the detubulated region. When the gap (detubulated region) was small, force generation was not appreciably affected due to the rapid propagation of the Ca^{2+} transient by diffusion and the slow time course of force development. By contrast, a large gap introduced a significant delay in the Ca^{2+} transient and in contraction in the detubulated region. Such dyssynchrony in contraction impairs the force generation and reduces the efficiency of contraction as the early contracting segment elongates the resting segment (internal shortening), thus wasting mechanical energy. These two factors may synergistically deteriorate cardiac function. In addition, our results suggest that the size of the detubulated region, together with t-tubule density, are the important factors for cardiomyocyte function, since the size of detubulation determines the delay of Ca^{2+} transient and the degree of inhomogeneity. In human heart failure there are

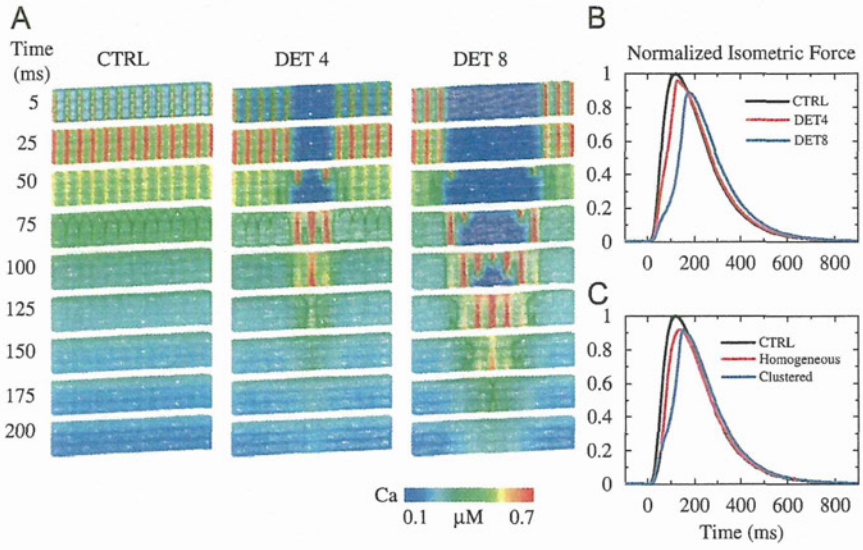

Fig. 7. Effect of regional detubulation on the Ca^{2+} transient and contraction. (A) Time-lapse images of $[Ca^{2+}]$ in color-coding during isometric contraction are shown for CTRL (left), DET4 (middle), and DET8 (right) myocytes. (B) Isometric forces are compared among the CTRL (black), DET4 (red), and DET8 (blue) myocytes. (C) Isometric forces are compared among the CTRL (black), homogeneous detubulation (red), and clustered detubulation (red). Forces are normalized for peak isometric value of CTRL in B and C.

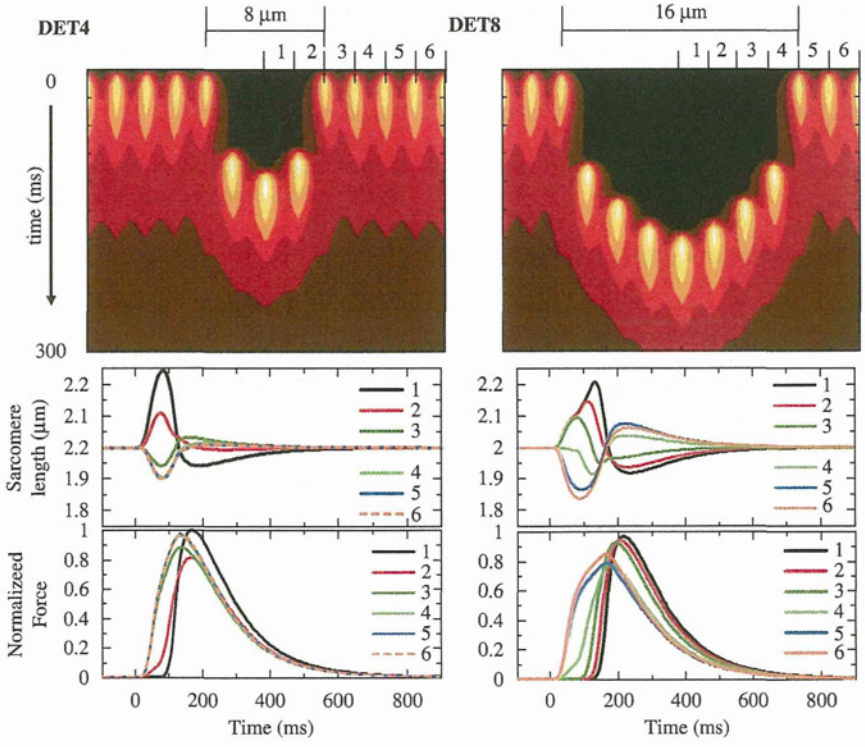

Fig. 8. Local Ca^{2+} transient and developed force of DET4 (left column) and DET8 (right column) models. Top rows: Longitudinal line-scan showing the local $[Ca^{2+}]$ with longitudinal position in horizontal axis and time after stimulus in vertical axis. Length change (middle rows) and developed force (bottom rows) of each sarcomere located in the position numbered in the longitudinal scan are shown.

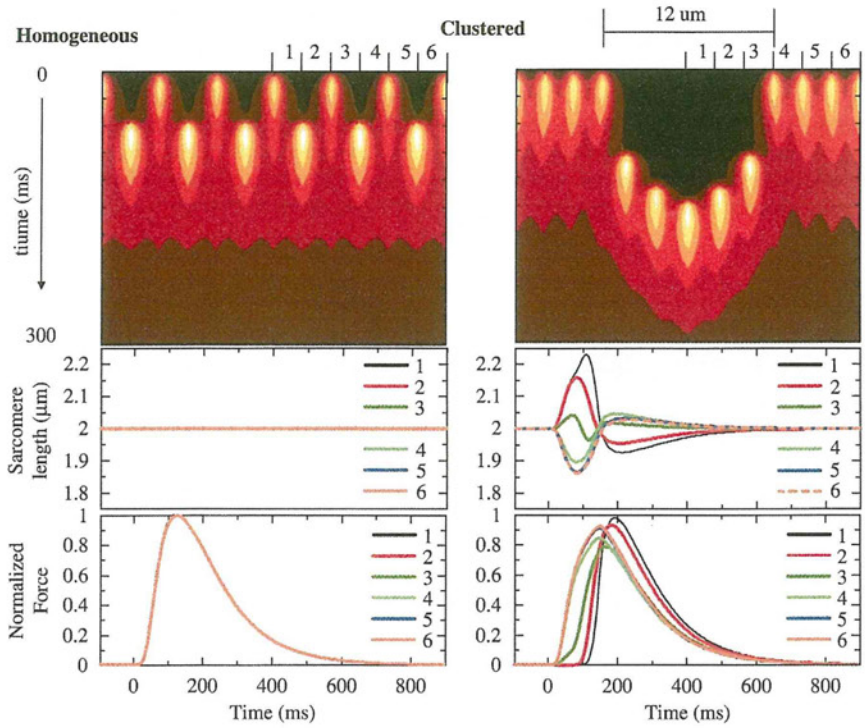

Fig. 9. Local Ca^{2+} transient and developed force of homogeneous (left column) and aggregated (right column) models. Top rows: Longitudinal line-scan showing the local $[Ca^{2+}]$ with longitudinal position in the horizontal axis and time after stimulus in the vertical axis. Length change (middle rows) and developed force (bottom rows) of each sarcomere located in the position numbered in the longitudinal scan are shown. In the homogeneous model, force and local $[Ca^{2+}]$ traces of each sarcomeres are superimposed.

large areas of t-tubule disorganization comparable to our large gap model (Fig. 5 of (Cannell et al., 2006)). However, in the murine model of heart failure the majority of the delayed Ca^{2+} release region had a width of less than 4 μm (Louch et al., 2006). Nevertheless, even with such small gaps in the t-tubule system, concomitant alterations in Ca^{2+} handling proteins can induce cardiac dysfunction. In this study, however, we only evaluated the effect of t-tubule disorganization.

4.3. Limitations of the model

For our model, we used both detailed single-sarcomere models and 12-sarcomere models with coarse mesh. However, even with the coarse mesh model, the analysis volume was insufficient to impose a three-dimensionally inhomogeneous deformation. A whole cell model with a more realistic sub-cellular structure is required for further analysis, although compromising the computational cost would be a prerequisite for such modeling. On the other hand, uncertainty in the subcellular distributions of functional components including ion channels also limits the analysis (Pasek et al., 2008). The modeling study can be used to estimate these unknown parameters, although further experimental clarification and verification are required. Finally, we assumed that the $[Ca^{2+}]$ of the t-tubular space was equal to that of bulk extracellular space. However, the $[Ca^{2+}]$ of t-tubular space was estimated to decrease by 13.8% at onset of Ca^{2+} release under pacing at 1 Hz (Pasek et al., 2008). The diffusion process in the extracellular space needs to be implemented in future model development.

Conflict of interest statement

None.

Acknowledgments

This research was supported by the Japan Society for the Promotion of Science (JSPS) through its Research Fellowships for Young Scientists (A.H.) and through its Funding Program for World-Leading Innovative R&D on Science and Technology FIRST Program (A.H., J.O., T.W., S.S., and T.H.), and JSPS KAKENHI (B) (20300152) (S.S.). This research was also supported by the Japan Science and Technology Agency (JST) through its University-Industry Collaborative Grants Fostering Innovation in Technology-Seeds.

Appendix A. Supplementary Information

Supplementary data associated with this article can be found in the online version at doi:10.1016/j.jbiomech.2011.11.022.

References

Aliev, M.K., Dos Santos, P., Hoerter, J.A., Soboll, S., Tikhonov, A.N., Saks, V.A., 2002. Water content and its intracellular distribution in intact and saline perfused rat hearts revisited. Cardiovascular Research 53, 48–58.

Bers, D.M., 2001. Ca source and Sinks. Excitation–Contraction Coupling and Cardiac Contractile Force, 2nd ed. Kluwer Academic Publishers, Dordrecht, The Netherlands.

Bers, D.M., 2006. Altered cardiac cyocyte Ca regulation in heart failure. Physiology 21, 380–387.

Brette, F., Despa, S., Bers, D.M., Orchard, C.H., 2005. Spatiotemporal characteristics of SR Ca^{2+} uptake and release in detubulated rat ventricular myocytes. Journal of Molecular and Cellular Cardiology 39, 804–812.

Brette, F., Komukai, K., Orchard, C.H., 2002. Validation of formamide as a detubulation agent in isolated rat cardiac cells. American Journal of Physiology 283, H1720–H1728.

Brette, F., Orchard, C., 2003. T-tubule function in mammalian cardiac myocytes. Cardiovascular Research 92, 1182–1192.
Brette, F., Rodriguez, P., Komukai, K., Colyer, J., Orchard, C.H., 2004. β-adrenergic stimulation restores the Ca transient of ventricular myocytes lacking t-tubule. Journal of Molecular and Cellular Cardiology 36, 265–275.
Cannell, M.B., Crossman, D.J., Soeller, C., 2006. Effects of changes in action potential spike configuration, junctional sarcoplasmic reticulum micro-architecture and altered t-tubule structure in human heart failure. Journal of Muscle Research and Cell Motility 27, 297–306.
Chen-Izu, Y., McCulle, S.L., Ward, C.W., Soeller, C., Allen, B.M., Rabang, C., Cannell, M.B., Balke, C.W., Izu, L.T., 2006. Three-dimensional distribution of ryanodine receptor clusters in cardiac myocytes. Biophysical Journal 91, 1–13.
Cheng, Y., Yu, Z., Hoshijima, M., Holst, M.J., McCulloch, A.D., McCammon, J.A., Michailova, A.P., 2010. Numerical analysis of Ca^{2+} signaling in rat ventricular myocytes with realistic transverse-axial tubular geometry and inhibited sarcoplasmic reticulum. PLoS Computational Biology 6, e1000972.
Cortassa, S., Aon, M.A., O'Rourke, B., Jacques, R., Tseng, H.-J., Marban, E., Winslow, R.L., 2006. A computational model integrating electrophysiology, contraction, and mitochondrial bioenergetics in the ventricular myocyte. Biophys J 91, 1564–1589.
de Graaf, R.A., van Kranenburg, A., Nicolay, K., 2000. In Vivo ^{31}P-NMR diffusion spectroscopy of ATP and phosphocreatine in rat skeletal muscle. Biophysical Journal 78, 1657–1664.
Dibb, K.M., Clarke, J.D., Horn, M.A., Richards, M.A., Graham, H.K., Eisner, D.A., Trafford, A.W., 2009. Characterization of an extensive transverse tubular network in sheep atrial myocytes and its depletion in heart failure. Circulation: Heart Failure, 482–489.
Greenstein, J.L., Hinch, R., Winslow, R.L., 2006. Mechanisms of excitation–contraction coupling in an integrative model of the cardiac ventricular myocyte. Biophysical Journal 90, 77–91.
Harris, D.M., Mills, G.D., Chen, X., Kubo, H., Berretta, R.M., Votaw, V.S., Santana, L.F., Houser, S.R., 2005. Alterations in early action potential repolarization causes localized failure of sarcoplasmic reticulum Ca^{2+} release. Circulation Research 96, 543–550.
Heinzel, F.R., Bito, V., Biesmans, L., Wu, M., Detre, E., von Wegner, F., Claus, P., Dymarkowski, S., Maes, F., Bogaert, J., Rademakers, F., D'hooge, J., Sipido, K., 2008. Remodeling of T-tubules and reduced synchrony of Ca^{2+} release in myocytes from chronically ischemic myocardium. Circulation Research 102, 338–346.
Ibrahim, M., Al Masri, A., Navaratnarajab, M., Siedlecka, U., Scopa, G.K., Moshkov, A., Al-Saud, S.A., Gorelik, J., Yacoub, M.H., Terraciano, C.M.N., 2010. Prolonged mechanical unloading affects cardiomyocyte excitation–contraction coupling, transverse-tubule structure, and the cell surface. FASEB Journal 24, 321–3329.
Kawai, M., Hussain, M., Orchard, C.H., 1999. Excitation–contraction coupling in rat ventricular myocyte after formamide-induced detubulation. American Journal of Physiology 277, H603–H609.
Kirk, M.M., Izu, L.T., Chen-Izu, Y., McCulle, S.L., Wier, W.G., Balke, C.W., Shorofsky, S.R., 2003. Role of the transverse-axial tubule system in generating calcium sparks and calcium transients in rat atrial myocytes. Journal of Physiology 547, 441–451.
Livshitz, L.M., Rudy, Y., 2007. Regulation of Ca^{2+} and electrical alternans in cardiac myocytes: role of CAMKII and repolarizing currents. American Journal of Physiology – Heart and Circulatory Physiology 292, H2854–H2866.
Louch, W.E., Bito, V., Heinzel, F.R., Macianskiene, R., Vanhaecke, J., Flameng, W., Mubagwa, K., Sipido, K.R., 2004. Reduced synchrony of Ca^{2+} release with loss of T-tubules – a comparison to Ca^{2+} release in human failing cardiomyocyte. Cardiovascular Research 62, 63–73.
Louch, W.E., Mork, H.K., Sexton, J., Stromme, T.A., Laake, P., Sjaastad, I., Sejersted, O.M., 2006. T-tubule disorganization and reduced synchrony of Ca^{2+} release in murine cardiomyocytes following myocardial infarction. Journal of Physiology 574, 519–533.
Lukyanenko, V., Chikando, A., Lederer, W.J., 2009. Mitochondria in cardiomyocyte Ca^{2+} signaling. The International Journal of Biochemistry & Cell Biology 41, 1957–1971.
Negroni, J.A., Lascano, E.C., 1996. A cardiac muscle model relating Sarcomere dynamics to calcium kinetics. Journal of Molecular and Cellular Cardiology 28, 915–929.
Okada, J., Sugiura, S., Nishimura, S., Hisada, T., 2005. Three-dimensional simulation of calcium waves and contraction in cardiomyocytes using the finite element method. American Journal of Physiology 288, 510–522.
Orchard, C., Brette, F., 2008. t-tubules and sarcoplasmic reticulum function in cardiac ventricular myocytes. Cardiovascular Research 77, 237–244.
Pasek, M., Simurda, J., Orchard, C.H., Christe, G., 2008. A model of the guinea-pig ventricular cardiac myocyte incorporating a transverse-axial tubular system. Progress in Biophysics and Molecular Biology 96, 258–280.
Smyrnias, I., Mair, W., Harzheim, D., Walker, S.A., Roderick, H.L., Bootman, M.D., 2010. Comparison of the T-tubule system in adult rat ventricular and atrial myocytes, and its role in excitation–contraction coupling and inotropic stimulation. Cell Calcium 47, 210–223.
Song, L.-S., Sobie, E.A., McCulle, S., Lederer, W.J., Balke, C.W., Cheng, H., 2006. Orphaned ryanodine receptors in the failing heart. Proceedings of the National Academy of Sciences of the United States of America 103, 4305–4310.
Stern, M.D., 1992. Theory of excitation–contraction coupling in cardiac muscle. Biophysical journal 63, 497–517.
Vendelin, M., Birkedal, R., 2008. Anisotropic diffusion of fluorescently labeled ATP in rat cardiomyocytes determined by raster image correlation spectroscopy. American Journal of Physiology 295, C1302–C1315.
Watanabe, H., Sugiura, S., Kafuku, H., Hisada, T., 2004. Multiphysics simulation of left ventricular filling dynamics Using fluid–structure interaction. Finite Element Method 87, 2074–2085.
Wei, S., Guo, A., Chen, B., Kutschke, W., Xie, Y.-P., Zimmerman, K., Weiss, R.M., Anderson, M.E., Cheng, H., Song, L.-S., 2010. T-tubule remodeling during transition from hypertrophy to heart failure. Circulation Research 107, 520–531.
Yang, A., Pascarel, C., Steele, D.S., Komukai, K., Brette, F., Orchard, C.H., 2002. Na^+–Ca^{2+} exchanger activity is localized in the T-tubules of rat ventricular myocytes. Circulation Research 91, 315–322.
Yu, Z., Yao, G., Hoshijima, M., Michailova, A., Holst, M., 2011. Multi-scale modeling of calcium dynamics in ventricular myocytes with realistic transverse tubules. Biomedical Engineering, IEEE Transactions on PP. 1-1.

34th Annual International Conference of the IEEE EMBS
San Diego, California USA, 28 August - 1 September, 2012

Exercise Training Plus Calorie Restriction Causes Synergistic Protection against Cognitive Decline via Up-regulation of BDNF in Hippocampus of Stroke-prone Hypertensive Rats

T. Kishi, K. Sunagawa

Abstract— **One of the important organ damage of hypertension is cognitive decline. Cognitive function is determined by the function of hippocampus, and previous studies have suggested that the decrease in brain-derived neurotrophic factor (BDNF) in the hippocampus causes cognitive decline. Protection against cognitive decline is reported not only in pharmacological therapy but also in exercise training or calorie restriction. The aim of the present study was to determine whether exercise training plus calorie restriction cause synergistic protection against cognitive decline via BDNF in the hippocampus or not. Exercise training for 28 days improved cognitive decline determined by Morris water maze test via up-regulation of BDNF in the hippocampus of stroke-prone spontaneously hypertensive rats, whereas calorie restriction for 28 days did not. However, exercise training plus calorie restriction causes the protection against cognitive decline to a greater extent than exercise training alone. In conclusion, exercise training plus calorie restriction causes synergistic protection against cognitive decline via up-regulation of BDNF in the hippocampus of stroke-prone hypertensive rats.**

I. Introduction

One of the important organ damages of hypertension and cardiovascular diseases is cognitive decline. Systemic oxidative stress and/or antioxidant deficiency cause cognitive decline [1], and especially, oxidative stress in hippocampus impairs cognitive function [2]. In the brain, brain-derived neurotrophic factor (BDNF) is known to be involved in the protective mechanisms against stress and cell death as an antioxidant [3-5]. In the hippocampus, BDNF protects against ischemic cell damage [6].

Not only the pharmacological therapy but also exercise training [7-9] or calorie restriction [10. 11] has been suggested to cause the protection against cognitive decline. Furthermore, calorie restriction improved cognitive function through the effects on hippocampus. However, in a previous clinical study, calorie restriction and/or exercise training did not protect against cognitive decline [12]. In hypertensive rats, it has not been determined whether calorie restriction protects against cognitive decline or not. The mechanisms in which exercise training and/or calorie restriction cause the protection against cognitive decline should be discussed more.

The aim of the present study was to determine whether exercise training plus calorie restriction causes synergistic protection against cognitive decline via up-regulation of BDNF in the hippocampus of stroke-prone hypertensive rats. To do this aim, we used stroke-prone spontaneously hypertensive rats (SHRSP), as hypertensive and vascular dementia model rats [13]. We divided SHRSP into 4 groups, SHRSP with exercise training (EX), SHRSP with calorie restriction (CR), SHRSP with exercise training plus calorie restriction (E+C), and control SHRSP (Ctl). Exercise training and/or calorie restriction were done for 28 days. Cognitive function was determined by Morris water maze test.

II. Methods

A. Animals

This study was reviewed and approved by the committee on ethics of Animal Experiments, Kyushu University Graduate School of Medical Sciences, and conducted according to the Guidelines for Animal Experiments of Kyushu University. Male SHRSP (12 to 14 week old), weighing 350 to 425 g and fed standard feed were used (SLC Japan, Hamamatsu, Japan). They were housed individually in a temperature-controlled room (22° to 23°C) with a 12-hour/12-hour light-dark cycle (lights on at 7:00 AM). We divided SHRSP into 4 groups, EX, CR, E+C, and Ctl (n=5 for each). Systolic blood pressure was measured dairy using the tail-cuff method (BP-98A; Softron, Tokyo, Japan).

B. Exercise Training

EX and E+C groups were submitted to a maximal exercise test on the treadmill (20 degree angle, 10 m/min for 30 minutes) every day for 28 days, as previously described [14].

C. Calorie Restriction

CR and E+C groups were given 70% of their mean 24-hour food intake. Food was given dairy 2-3 hours before lights off. EX and control groups were free to have food, as previously described [15].

D. Western Blotting Analysis

At the end of the protocol, to obtain the hippocampus tissues, the rats were deeply anesthetized with sodium pentobarbital (100 mg/kg IP) and perfused transcardially with PBS (150 mol/L NaCl, 3 mmol/L KCl, and 5 nmol/L

T. Kishi is with the Department of Advanced Therapeutics for Cardiovascular Diseases, Kyushu University Graduate School of Medical Sciences, Fukuoka 812-8582, Japan (corresponding author to provide phone: +81-92-642-5360; fax: +81-92-642-5374; e-mail: tkishi@cardiol.med.kyushu-u.ac.jp).

K. Sunagawa was with the Department of Cardiovascular Medicine, Kyushu University Graduate School of Medical Sciences, Fukuoka 812-8582, Japan (e-mail: sunagawa@cardiol.med.kyushu-u.ac.jp).

978-1-4577-1787-1/12/$26.00 ©2012 IEEE

phosphate; pH 7.4, 4°C). The brains were removed quickly, and sections 1 mm thick were obtained with a cryostat at –7±1°C. The hippocampus defined according to a rat brain atlas and obtained by a punch-out technique, and the hippocampus tissues were homogenized and then sonicated in a lysing buffer containing 40 mmol/L HEPES, 1% Triton X-100, 10% glycerol, and 1 mmol/L phenylmethanesulfonyl fluoride. The tissue lysate was centrifuged at 6000 rpm for 5 minutes at 4°C with a microcentrifuge. The lysate was collected, and protein concentration was determined with a BCA protein assay kit (Pierce). An aliquot of 20 μg of protein from each sample was separated on 12% SDS-polyacrylamide gel. Proteins were subsequently transferred onto polyvinylidene difluoride membranes (Immobilon-P membrane; Millipore). Membranes were incubated for 2 hours with a rabbit polyclonal antiserum against BDNF (1:1000; Abcam, Cambridge, UK) or α-tubulin (1:1000; Cell Signaling). Membranes were then washed and incubated with a horseradish peroxidase–conjugated horse anti-mouse IgG antibody (1:10000) for 40 minutes. Immunoreactivity was detected by enhanced chemiluminescence autoradiography (plus Western blotting detection kit; Amersham), and was expressed as the ratio to β-tubulin protein.

E. Morris Water Maze Test

Spatial leaning and memory function of the rats were investigated with the Morris water maze test in a circular pool filled with water at a temperature of 25.0±1°C [16]. In the hidden platform test, a transparent platform was submerged 1cm below the water level. Swimming paths were tracked with a camera fixed on the ceiling of the room and stored in a computer. All the procedures of the Morris water maze were performed for 7 days. A pre-training session was carried out at day 0, in which animals were given 60 seconds free swimming without the platform. In the hidden-platform test for 4 days, the rats were given 2 trials (1 session) on day 1 and 4 trials (2 sessions) per day on day 2, 3, and 4. The initial trial interval was about 30 min and the inter-session interval was 2 hours. During each trial, the rats were released from four pseudo-randomly assigned starting points and allowed to swim for 60 seconds. After mounting the platform, the rats were allowed to remain there for 15 seconds, and were then placed in the home cage until the start of the next trial. If a rat was unable to find the platform within 60 seconds, it was guided to the platform and allowed to rest on the platform for 15 seconds. Probe trials were performed at day 5. In the probe trial, the hidden platform was removed and the rats was released from the right quadrant and allowed to swim freely for 60 seconds. The time spent in the target quadrant, where the platform has been located during training, and the time spent in the other quadrants were measured. In the visible-platform test was performed at day 6, the platform was elevated above the water surface and placed in a different position. The rats were given for trials with an inter-trial interval of 10 minutes.

F. Statistical Analysis

All values are expressed as mean ± SEM. Comparisons between any two mean values were performed using Bonferroni's correction for multiple comparisons. ANOVA was used to compare all the parameters in all groups. Differences were considered to be statistically significant at a P value of <0.05.

III. Results

A. Blood Pressure

Systolic blood pressure was reduced to the similar levels in EX and E+C, and was significantly lower in EX and E+C than in Ctl (Fig. 1). Systolic blood pressure was not different between in CR and Ctl (Fig. 1).

B. BDNF in the Hippocampus

The expression of BDNF in the hippocampus was significantly higher in E+C than in Ctl to a greater extent than in EX (Fig. 2). However, the expression of BDNF in the hippocampus was not different between in CR and Ctl (Fig. 2).

C. Morris Water Maze Test

In the hidden platform test, escape latency was significantly lower in E+C than in Ctl to a greater extent than in EX (Fig. 3A). However, escape latency was not different in CR and Ctl (Fig. 3A). In the probe test, E+C resulted in significantly more time in the target quadrant as compared with EX, CR, and Ctl (Fig. 3B). In the visible platform test, there were no significant differences in escape latency among all of the groups.

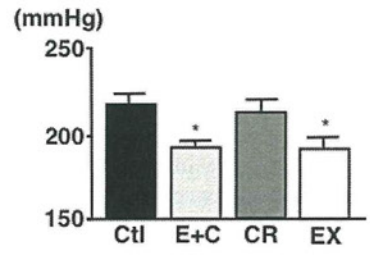

Figure 1. Systolic blood pressure in each groups. *P<0.05 versus Ctl, n=5 for each. Abbreviations; Ctl, control; E+C. exercise training+calorie restriction; CR, calorie restriction; EX, exercise training.

IV. Discussion

In the present study, we demonstrated that exercise training plus calorie restriction improves cognitive performance and increases BDNF in the hippocampus of SHRSP to a greater extent than exercise training alone. However, calorie restriction alone did not have such effects.